Contributions to Mineralogy and Petrology (2026) 181:40
https://doi.org/10.1007/s00410-026-02309-w

ORIGINAL PAPER

Phase equilibria and liquid lines of descent in alkali basalts at one atmosphere and the role of oxygen fugacity

Sophia Y. M. Thorn[1] · Olivier Namur[1] · David A. Neave[2] · Bernard Charlier[3] · Jasper Berndt[4] · Stephan Klemme[4]

Received: 7 August 2025 / Accepted: 26 February 2026

Abstract

This study presents new experimental data on the effect of oxygen fugacity (fO_2) and bulk composition on phase equilibria and liquid lines of descent in alkali basalts. Crystallisation experiments were performed at one atmosphere, in the temperature range 1220–1050 °C and at fO_2 conditions corresponding to fayalite–magnetite–quartz (FMQ) equilibrium and the following log-unit deviations from this equilibrium: FMQ-1, FMQ + 1.5 and FMQ + 3. Experiments were grouped into two series, those on primitive compositions (9.9–11.9 wt% MgO; total alkali 3.1–5.3 wt%), and those on evolved compositions (5.1–5.8 wt% MgO; total alkali 5.7–8.6 wt%). Experiments on primitive compositions produce assemblages of olivine, clinopyroxene and spinel, with plagioclase present in less silica-undersaturated compositions. Experiments on evolved compositions produce similar assemblages, though olivine is often absent at higher fO_2. Whitlockite is present at low temperature, plus occasional Fe-Ti oxides. Nepheline is only observed in the most silica-undersaturated composition at low temperature. Mineral compositions and stability are strongly controlled by bulk composition and redox conditions. High MgO bulk contents favour the early appearance of olivine, while the appearance of clinopyroxene is dictated by both MgO and CaO contents. Increasing silica-undersaturation produces assemblages dominated by clinopyroxene and a high melt fraction at any given temperature, promoting alkali enrichment during melt evolution. Oxidising conditions enhance the crystallisation of spinel and other Fe-Ti oxides, in which both silica and alkalis are incompatible, through increased melt $Fe^{3+}/\Sigma Fe$. This promotes more modest enrichments in Na_2O and K_2O with respect to SiO_2 as crystallisation proceeds, with the effect strongest where bulk concentrations of FeO_{tot} are high and P_2O_5 are low. It follows that fO_2 exerts a stronger control over the liquid lines of descent of more primitive liquids than evolved ones. We combine our results with those from the literature to calibrate new models for both $K_{D_{Fe^{2+}-Mg}}^{Ol-Melt}$ and $K_{D_{Fe^{T}-Mg}}^{Ol-Melt}$ in alkaline systems, with the latter formulated as:

$$K_{D_{Fe^{T}-Mg}}^{Ol-Melt}(\pm 0.012, \text{a.a.d.}) = 0.442\,(\pm 0.029) + 0.287\,(\pm 0.035)\,[X_{SiO_2}] - 0.442\,(\pm 0.027)\left[\frac{X_{Na_2O} + X_{K_2O}}{X_{SiO_2}}\right] - 0.168\,(\pm 0.022)\,[X_{Fo}] - 0.138(\pm 0.008)\frac{1}{(1 - \left[\frac{Fe^{3+}}{\Sigma Fe}\right])}$$

where X_i is the mole fraction of i in the melt, X_{Fo} is molar MgO/(MgO + FeO_{tot}) of olivine, $Fe^{3+}/\Sigma Fe$ represents Fe valence in the melt and a.a.d. is the average absolute deviation. We also present a simple model for estimating $K_{D_{Fe^{T}-Mg}}^{Cpx-Melt}$:

$$K_{D_{Fe^{T}-Mg}}^{Cpx-Melt}(\pm 0.028, \text{a.a.d.}) = -1.00\,(\pm 0.064) + 2.129\,(\pm 0.063)\left[\frac{T\ (^{\circ}C)}{1000}\right] - 1.675\,(\pm 0.021)\,[Mg\#] + 0.144(\pm 0.006)\frac{1}{1 - \left[\frac{Fe^{3+}}{\Sigma Fe}\right]}$$

Communicated by Othmar Müntener.

✉ Sophia Y. M. Thorn
saffy.thorn@kuleuven.be

[1] Department of Earth and Environmental Sciences, KU Leuven, 3000 Leuven, Belgium

[2] Department of Earth and Environmental Sciences, University of Manchester, Manchester M13 9PL, UK

[3] Department of Geology, University of Liège, 4000 Sart Tilman, Belgium

[4] Institute for Mineralogy, University of Münster, 48149 Münster, Germany

Published online: 05 May 2026

where Mg# is molar MgO/(MgO + FeO_{tot}) of clinopyroxene and $Fe^{3+}/\Sigma Fe$ represents Fe valence in the melt. These new formulations allow equilibrium $K_{D_{Fe-Mg}}^{Mineral-Melt}$ to be estimated more reliably in oxidising, alkaline systems where $Fe^{3+}/\Sigma Fe$ is high.

Keywords Oxygen fugacity · Experimental petrology · Crystallisation experiments · Alkali magmas · Silica-undersaturation

Introduction

Oxygen fugacity, fO_2, the oxygen partial pressure corrected for the non-ideality of the gas, is an intensive parameter used to describe redox state in a given geological system, i.e. the potential of a given multivalent element to occur in a more oxidised or reduced state (Frost 1991; Moretti and Neuville 2021). Redox state exerts a strong control over the evolution of minerals and magmatic liquids during progressive cooling and crystallisation, alongside pressure, temperature, bulk composition and volatile content (Sisson and Grove 1993; Toplis and Carroll 1995; Müntener et al. 2001; Villiger et al. 2007; Conte et al. 2009; Markl et al. 2010). This is a direct result of its influence over the $Fe^{3+}/\Sigma Fe$ ratio of melts, and hence the composition and stability of Fe-bearing phases (Osborn 1959; Kress and Carmichael 1991; Toplis and Carroll 1995, 1996).

The potential for differences in redox to produce variable liquid lines of descent in subalkaline systems has been demonstrated experimentally by numerous authors since the 1950s. This includes work at 1 bar (e.g. Hill and Roeder 1974; Snyder et al. 1993; Toplis and Carroll 1995; Zhang et al. 2023) and under pressure (e.g. Hamilton et al. 1964; Berndt et al. 2005; Feig et al. 2010; Ulmer et al. 2018). Alkali magmas are comparatively understudied in this regard, with those studies that do exist often restricted to one or two compositions (e.g. Duke 1971; Salazar-Naranjo and Vlach 2023), only one fO_2, typically equivalent to the fayalite–magnetite–quartz (FMQ) equilibrium (e.g. Sack et al. 1987; Gee and Sack 1988; Thy and Lofgren 1994; Gerke et al. 2005), or have focused on other important parameters such as pressure, volatile content and the effect of fractional crystallisation (e.g. Nekvasil et al. 2004; Pilet et al. 2010; Conte et al. 2009). However recent thermodynamic modelling in dry alkaline systems has served to highlight the complex relationships between melt Fe^{3+} content, fO_2 and temperature, all of which directly affect the compositional evolution of melts and minerals (Weller et al. 2024; Soderman et al. 2025).

Alkali magmas are widely observed in rift systems, subduction zones and at ocean islands. Despite their volumetric insignificance compared to subalkaline magmas, alkali magmas are of increasing scientific and economic interest; their propensity to concentrate critical minerals (i.e. highly incompatible trace elements) such as the rare earth elements (Goodenough et al. 2016; Beard et al. 2023), makes them vital for delivering the energy transition. Alkali magmas are highly diverse in terms of mineralogy and composition, and range from highly silica-undersaturated (e.g. Nyiragongo volcano, DRC; Molendijk et al. 2024) to silica-oversaturated (e.g. Bouvet Island; Jeffery and Gertisser 2018).

The presence of alkaline magmas at differing tectonic settings leads them to record evolution under different fO_2 conditions (Moussallam et al. 2019; Cottrell et al. 2021) (Fig. 1). In particular, primitive ocean island basalts (OIB) found at plume settings are known to record oxygen fugacities spanning three log units (FMQ 0.5 ± 1.5 (2sd); Willhite et al. 2024). Processes such as degassing (Cottrell and Kelley 2011; Cottrell et al. 2021; Brounce et al. 2017; Sossi et al. 2019; Connors et al. 2025), and the separation of Fe-bearing phases via crystal-liquid fractionation (Brounce et al. 2017) then further widen the spectrum of fO_2 conditions observed.

Here we present the results of one-atmosphere, high-temperature, phase equilibria experiments at a range of fO_2 conditions chosen to reflect those recorded in alkali magmas (Fig. 1). We investigate both MgO-rich primitive magmas and MgO-poor evolved magmas. These experiments were performed on nine alkali basalts from Fogo (Cape Verde), Terceira (Azores), Tristan da Cunha, Nyiragongo (Democratic Republic of the Congo) and Nyamulagira (Democratic Republic of the Congo), and represent three ocean islands and two localities in the East African continental rift. Our experiments were designed to systematically evaluate how key compositional parameters (e.g. alkalis, MgO, SiO_2, CaO) and fO_2 have the potential to produce lithological and mineralogical diversity.

We find that oxidising fO_2 conditions enhance the crystallisation of phases in which both alkalis and silica are incompatible, such as spinel, which promotes liquid lines of descent with lower enrichment in Na_2O and K_2O as a function of increasing SiO_2. These LLDs are enriched in silica relative to those produced at lower fO_2, an effect that is strongest in primitive compositions containing higher FeO_{tot}. At lower fO_2, the evolution of the melt is predominantly controlled by phases close in silica content to the melt, with

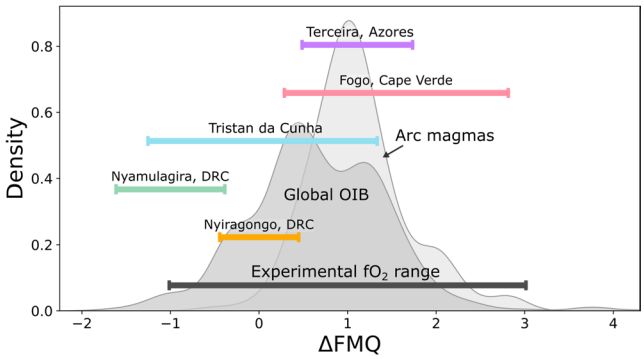

Fig. 1 Kernel density plot showing the distribution of fO_2 values relative to the fayalite–magnetite–quartz (FMQ) buffer measured in global OIBs, with the reported range of fO_2 for starting composition localities overlain (Anderson 1968; Mata et al. 2017; Head et al. 2018; Moussallam et al. 2019; Klügel et al. 2020; Nicklas et al. 2022; DeVitre et al. 2023; Shepherd 2024; Connors et al. 2025), along with the range of fO_2 explored in this study. Sources for global OIB and arc magma estimates are provided in Supplementary Material 1

much lower alkali content, such as clinopyroxene, leading to alkali enrichment. While most natural alkaline magmas are typically volatile bearing and are formed under pressure, our results are an essential step towards understanding the controls over magmatic differentiation in alkaline systems, and may be used as calibration data to improve existing models for application to these enigmatic magmatic systems (e.g., Ghiorso and Sack 1995; Weller et al. 2024).

Experimental techniques

Starting material

We chose experimental starting compositions with a range of alkali contents, in order to test the effect of alkalinity on the phase equilibria and evolution trajectory of any given melt. To do this, nine natural starting compositions were chosen from localities known to erupt alkali-rich products: Fogo (Cape Verde; Hildner et al. 2012), Terceira (Azores; Shepherd 2024), Tristan da Cunha (Le Roex et al. 1990), Nyiragongo (Democratic Republic of the Congo; Molendijk et al. 2024) and Nyamulagira (Democratic Republic of the Congo; Kamate Kaleghetso et al. 2025). One sample from Fogo (FO22-048) was specifically collected for this study during a field mission in 2022. From these localities, five primitive compositions with MgO content of 9.9–11.9 wt% (Mg#: 58.42 to 63.15, with Mg# being molar [100·Mg/(Mg+Fe_{tot})], where Fe_{tot} = total Fe; total alkali 3.1–5.3 wt%; alkalinity index (AI) 0.33–0.62, with AI being molar [(Na_2O+K_2O)/Al_2O_3]) and four evolved compositions with MgO contents of 5.2–5.8 wt% (Mg# 46.12–50.67; total alkali 5.7–8.6 wt%; AI 0.55–0.81) were chosen. Within both the primitive and evolved groups, we selected samples that vary in terms of alkali and silica content, and degree of silica-undersaturation. This enabled us to explore the effect of these parameters, alongside fO_2, in producing lithological and mineralogical diversity at different stages of melt evolution.

Whole-rock samples were finely ground and homogenized in an agate ball mill, fused at 1400 °C under air in an iron-saturated Pt crucible to minimise Fe-loss, and quenched in water. Resultant glasses were examined using a Scanning Electron Microscope (SEM; see details below) to check for compositional homogeneity and to ensure that no crystals were present. They were then reground in ethanol for 1 h using a Pulverisette 2 mortar grinder to produce a homogenous powder. It was not possible to melt sample FOGO16 due to limited available quantities of starting material, so this composition was ground multiple times to ensure homogeneity, and the starting composition determined via XRF by Hildner et al. (2012) was used (Table 1).

Experimental methods

All experiments were performed in a Nabertherm RHTV 50/150/17 vertical tube furnace at KU Leuven, Belgium. Experimental powders were fused onto 0.2 mm diameter Pt-loops by heating to super-liquidus temperatures (1400 °C) in a muffle furnace for 3 min. Experimental charges were then suspended in the vertical furnace hotspot, with multiple compositions run at the same time. Temperatures were measured using an S-type (Pt-$Pt_{90}Rh_{10}$) thermocouple, calibrated against the melting points of Ag and Au, located above the samples. Loops were pre-saturated in Fe by running a prior experiment at similar temperature and fO_2 conditions to each actual experiment for at least 24 h to limit Fe loss, with material on the loops mechanically broken off prior to use.

Most experiments were run under isothermal conditions. However, low-temperature experiments (primitive starting compositions: ≤1120 °C FMQ+3; evolved starting compositions: ≤1095 °C FMQ+3, ≤1074 °C FMQ-1 and FMQ+1.5, ≤1050 °C FMQ) were held at the target temperature for 1 h, before applying thermal oscillations of +10 °C above the target temperature for the first 10 h of the experiment, to promote the growth of large crystals and melt pools (Erdmann and Koepke 2016). Temperature intervals between experiments were selected to enable the saturation temperature of different phases to be bracketed as closely as possible across all compositions. We chose to run experiments at oxygen fugacities ranging from FMQ to FMQ+3 on all compositions in order to reflect the fO_2 conditions recorded in naturally occurring alkaline magmas (Fig. 1; Cottrell et al. 2021). Due to the potential for self-reduction

Table 1 Major element composition of the experimental starting materials, normalised to 100 wt%

Locality	Primitive					Evolved			
	Terceira, The Azores	Tristan da Cunha	Fogo, Cape Verde	Nyamulagira, DRC	Nyiragongo, DRC	Terceira, The Azores	Fogo, Cape Verde	Nyamulagira, DRC	Nyiragongo, DRC
wt.%	AZKS052	TDC69	FOGO16	NM20ON179	NY17-209	AZKS003	FO22-048	NM19ON009	NY17-219
SiO_2	47.85	43.20	43.71	45.32	40.18	50.30	44.72	48.46	44.44
TiO_2	2.91	3.19	3.26	3.06	3.57	2.97	3.48	2.96	2.83
Al_2O_3	14.30	11.77	12.87	12.65	11.70	15.37	16.71	16.57	16.19
FeO_{tot}	10.32	14.36	12.48	10.75	12.70	10.15	10.51	9.41	10.72
MnO	0.16	0.16	0.22	0.19	0.23	0.19	0.20	0.18	0.23
MgO	9.91	11.89	10.15	10.34	10.01	5.78	5.52	5.42	5.15
CaO	10.87	11.08	13.44	12.37	15.19	8.23	10.27	8.48	10.61
Na_2O	2.48	2.24	1.94	2.39	2.73	4.21	4.34	3.67	6.66
K2O	0.58	1.59	1.12	2.32	2.53	1.50	3.14	4.01	1.94
P_2O_5	0.50	0.46	0.81	0.50	1.05	1.23	1.08	0.81	1.20
Cr_2O_3	0.02	0.02	–	0.04	0.04	0.02	0.01	0.01	0.03
NiO	0.10	0.04	–	0.08	0.06	0.05	0.02	0.03	0.01
Mg#	63.14	59.61	59.19	63.15	58.42	50.37	48.37	50.67	46.12

Cr_2O_3 and NiO were not measured in sample FOGO16. Mg# is calculated as molar [100·Mg/(Mg+Fe_{tot})]. Sample TDC69 obtained from Le Roex et al. (1990), FOGO16 from Hildner et al. (2012), AZKS052 and AZKS003 from Shepherd (2024), NM20ON179 and NM19ON009 from Kamate Kaleghetso et al. (2025) and NY17-209 and NY17-219 from Molendijk et al. (2024). FO22-048 was collected for this study during fieldwork in 2022

of alkaline magmas, through crystallisation of sodic amphiboles and pyroxenes which incorporate Fe^{3+} (Markl et al. 2010), we performed further experiments at FMQ-1 on evolved starting compositions. fO_2 was calculated using the thermodynamic data of Chase et al. (1985), and the position of the FMQ buffer at 1 bar was determined using the equation of O'Neill (1987). Oxygen fugacity was buffered by flushing the tube with high-purity mixtures of CO_2 and CO gases, controlled via Bronkhorst gas-flow controllers, operating at a flow rate of 50 cm^3/min for experiments performed between FMQ-1 and FMQ+1.5, and 150 cm^3/min for those at FMQ+3. We chose to use a fairly modest gas flow as a measure to reduce alkali-loss. A higher flow rate was necessary at FMQ+3 to enable precise control over the small proportion of CO gas required at these conditions. The accuracy of fO_2 conditions by CO-CO_2 mixing was tested using electromotive force (emf) measurements with an yttria-stabilized zirconia electrolyte cell with the reference chemical potential of O_2 corresponding to air (XO_2=0.21). Accuracy was found to be better than 0.1 log unit. Experiments were rapidly quenched by dropping charges into water. Run products were then removed from their Pt-loops and mounted in epoxy for analysis. The experimental run conditions, run products and phase proportions are reported in Table 2.

Analytical methods and calculations of melt and mineral compositions and components

Experimental products were imaged using either a TESCAN Mira 4 field emission gun-scanning electron microscope (FEG-SEM) at the Department of Earth and Environmental Sciences, KU Leuven, Belgium, or a JEOL JXA-8530F field emission electron probe microanalyser (EPMA) at the Department of Materials, KU Leuven, Belgium.

Starting glasses and experimental charges were analysed using a JEOL JXA-8530F EPMA at the Institute for Mineralogy at the University of Münster, Germany, and the Department of Materials, KU Leuven, Belgium. Average compositions are reported in Tables S2–S7 (Supplementary Material 3). Operating conditions were 15 kV for all analyses, with 5–10 nA beam currents for glasses and 15–20 nA for minerals, excluding clinopyroxene which was measured with 40 nA. Glasses were analysed using a defocused beam (8–10 µm diameter) and minerals with a focused beam. Si, Ti, Al, Fe, Mn, Mg, Ca, Na, K, P, Cr and Ni were measured in glasses, olivine and clinopyroxene, while a subset of these elements was measured for the remaining minerals; further details are provided in Table S1 (Supplementary Material 3). Natural and synthetic primary standards were used for calibration (listed in Table S1, Supplementary Material 3), while secondary reference materials were measured at regular intervals, every 30–50 points, to ensure consistency between analytical sessions and to check accuracy and precision. The following reference materials were used: VG2 (NMNH 111240-52), San Carlos Olivine (NMNH

Table 2 Experimental conditions, phase assemblages and calculated phase proportions

Run	T (°C)	log fO_2	ΔFMQ	CO (ml/min)	CO2 (ml/min)	Duration (h)	Run products	ΣR^2	Fe-loss [%]	Na-loss [%]
AZKS052										
A1	1201	− 8.40	0	2.35	47.7	18	Gl (98.0), Ol (2.0)	0.79	4.2	4.3
A2	1170	− 8.77	0	2.21	47.8	26	Gl, Ol, Sp[a]			
A3	1141	− 9.13	0	2.07	47.9	46	Gl, Ol, Cpx, Sp[a]			
A3-5	1119	− 9.41	0	1.97	48	68	Gl, Ol, Cpx, Sp[a]			
A4	1109	− 9.55	0	1.92	48.1	71	Gl (46.7), Ol (13.6), Cpx (12.9), Pl (26.8), Sp (0.03)	0.51	1.4	0.6
B4	1201	− 6.90	1.5	0.43	49.6	22	Gl, Sp[a]			
B5	1169	− 7.28	1.5	0.41	49.6	42	Gl, Ol, Sp[a]			
B1	1139	− 7.66	1.5	0.38	49.6	70	Gl, Ol, Cpx, Pl, Sp[a]			
B2	1118	− 7.93	1.5	0.36	49.6	69	Gl (53.8), Ol (11.8), Cpx (10.1), Pl (24.1), Sp (0.1)	0.39	5.8	1.7
B3	1099	− 8.18	1.5	0.34	49.7	94	Gl (38.0), Ol (12.8), Cpx (16.1), Pl (32.0), Sp (1.1)	0.37	0.3	1.2
D4	1221	− 5.17	3	0.24	149.8	24	Gl (99.8), Sp (0.2)	1.00	0.6	4.8
D5	1201	− 5.40	3	0.23	149.8	23	Gl (99.8), Sp (0.2)	0.99	0.8	4.8
D1	1170	− 5.77	3	0.22	149.8	32	Gl (95.4), Ol (4.0), Sp (0.6)	0.97	0.4	5.9
D2	1140	− 6.14	3	0.20	149.8	65	Gl (72.7), Ol (9.2), Cpx (2.4), Pl (15.5), Sp (0.2)	0.35	2.5	1.9
D3	1120[b]	− 6.40	3	0.19	149.8	70	Gl (36.9), Ol (9.1), Cpx (18.7), Pl (31.1), Sp (2.6), Psb (1.4)	0.23	4.9	1.4
D6	1101[b]	− 6.65	3	0.18	149.8	93	Gl (18.8), Ol (8.5), Cpx (28.2), Pl (38.7), Sp (3.4), Psb (2.3)	0.25	9.1	1.3
FOGO16										
A1	1199	− 8.42	0	2.35	47.7	24	Gl (96.9), Ol (3.1)	0.60	10.3	16.0
A2	1169	− 8.78	0	2.20	47.8	26	Gl, Ol, Sp[a]			
A3	1141	− 9.13	0	2.07	47.9	46	Gl, Ol, Sp[a]			
A3-5	1119	− 9.41	0	1.97	48	68	Gl, Ol, Cpx, Pl, Sp[a]			
A4	1109	− 9.55	0	1.92	48.1	71	Gl (54.3), Ol (9.4), Cpx (23.1), Pl (12.7), Sp (0.4)	0.24	5.1	5.3
B4	1201	− 6.90	1.5	0.43	49.6	22	Gl (97.7), Ol (2.3)	0.53	9.6	9.3
B5	1169	− 7.28	1.5	0.41	49.6	42	Gl (94.3), Ol (5.4), Sp (0.1)	0.41	7.8	7.8
B1	1139	− 7.66	1.5	0.38	49.6	70	Gl, Ol, Cpx, Pl, Sp[a]			
B3	1099	− 8.18	1.5	0.34	49.7	94	Gl (21.2), Ol (4.9), Cpx (38.8), Pl (26.2), Sp (8.9)	0.60	12.8	0.6
D4	1221	− 5.17	3	0.24	149.8	24	Gl, Sp[a]			
D5	1201	− 5.40	3	0.23	149.8	23	Gl (99.2), Sp (0.8)	0.79	1.5	4.4
D1	1170	− 5.77	3	0.22	149.8	32	Gl, Ol[a], Sp			
D2	1140	− 6.14	3	0.20	149.8	65	Gl (61.6), Ol (4.3), Cpx (24.3), Pl (6.1), Sp (3.7)	0.33	3.7	8.0
D3	1120[b]	− 6.40	3	0.19	149.8	70	Gl (35.6), Ol (4.1), Cpx (35.7), Pl (18.0), Sp (6.5)	0.44	6.6	7.1
D6	1101[b]	− 6.65	3	0.18	149.8	93	Gl (17.8), Ol (1.3), Cpx (43.8), Pl (25.6), Sp (11.5)	0.83	0.1	8.9
TDC69										
A1	1199	− 8.42	0	2.35	47.7	21	Gl, Ol, Sp[a]			
A2	1170	− 8.77	0	2.21	47.8	26	Gl, Ol, Sp[a]			
A3	1141	− 9.13	0	2.07	47.9	46	Gl, Ol, Sp[a]			
A3-5	1119	− 9.41	0	1.97	48	68	Gl 73.7), Ol (16.6), Cpx (9.7), Sp (0.1)	0.63	1.1	5.2
A4	1109	− 9.55	0	1.92	48.1	71	Gl (62.1), Ol (16.2), Cpx (16.0), Pl (5.5), Sp (0.2)	0.77	3.1	7.9
B4	1201	− 6.90	1.5	0.43	49.6	22	Gl (90.2), Ol (9.3), Sp (0.5)	0.66	1.1	8.4
B5	1169	− 7.28	1.5	0.41	49.6	42	Gl (87.1), Ol (11.8), Sp (1.1)	0.70	3.3	13.3
B1	1139	− 7.66	1.5	0.38	49.6	70	Gl (82.5), Ol (14.5), Cpx (2.0), Sp (1.0)	0.37	3.6	9.4

Table 2 (continued)

Run	T (°C)	log fO_2	ΔFMQ	CO (ml/min)	CO2 (ml/min)	Duration (h)	Run products	ΣR^2	Fe-loss [%]	Na-loss [%]
B2	1118	− 7.93	1.5	0.36	49.6	69	Gl (57.1), Ol (13.1), Cpx (22.0), Pl (3.3), Sp (4.5)	0.30	5.2	2.8
B3	1099	− 8.18	1.5	0.34	49.7	94	Gl[a], Ol, Cpx[a], Sp			
D4	1221	− 5.17	3	0.24	149.8	24	Gl (93.3), Ol (5.6), Sp (1.1)	0.55	1.9	6.2
D5	1201	− 5.40	3	0.23	149.8	23	Gl (91.1), Ol (7.7), Sp (1.2)	0.61	1.3	7.9
D1	1170	− 5.77	3	0.22	149.8	32	Gl (87.0), Ol (9.8), Sp (3.2)	0.71	0.4	4.7
D2	1140	− 6.14	3	0.20	149.8	65	Gl (69.5), Ol (9.7), Cpx (14.7), Sp (6.1)	0.45	1.1	8.5
D3	1120[b]	− 6.40	3	0.19	149.8	70	Gl (45.7), Ol (8.24), Cpx (34.0), Pl (5.0), Sp (7.1)	0.44	6.1	8.5
D6	1101[b]	− 6.65	3	0.18	149.8	93	Gl[a], Ol, Cpx[a], Pl, Sp			
NM20ON179										
A1	1201	− 8.40	0	2.35	47.7	18	Gl (94.4), Ol (5.6)	0.60	5.0	16.8
A2	1170	− 8.77	0	2.21	47.8	26	Gl (92.3), Ol (7.7)	0.46	4.4	11.8
A3	1141	− 9.13	0	2.07	47.9	46	Gl, Ol, Cpx, Sp[a]			
A3-5	1119	− 9.41	0	1.97	48	68	Gl, Ol, Cpx, Sp[a]			
A4	1109	− 9.55	0	1.92	48.1	71	Gl, Ol, Cpx, Sp[a]			
B4	1201	− 6.90	1.5	0.43	49.6	22	Gl, Ol, Sp[a]			
B5	1169	− 7.28	1.5	0.41	49.6	42	Gl, Ol, Sp[a]			
B1	1139	− 7.66	1.5	0.38	49.6	70	Gl (76.3), Ol (7.4), Cpx (16.0), Sp (0.3)	0.59	11.1	4.3
B2	1118	− 7.93	1.5	0.36	49.6	69	Gl (66.3), Ol (7.1), Cpx (25.0), Sp (1.5)	0.50	2.7	4.3
B3	1099	− 8.18	1.5	0.34	49.7	94	Gl (48.0), Ol (7.3), Cpx (37.0), Pl (4.9), Sp (2.8)	0.43	2.4	4.2
D4	1221	− 5.17	3	0.24	149.8	24	Gl (100.0)	0.95	2.9	8.4
D5	1201	− 5.40	3	0.23	149.8	23	Gl (96.3), Ol (3.7)	0.80	1.9	11.8
D1	1170	− 5.77	3	0.22	149.8	32	Gl, Ol, Cpx[a], Sp			
D2	1140	− 6.14	3	0.20	149.8	65	Gl (70.5), Ol (5.6), Cpx (21.9), Sp (1.9)	0.58	1.5	6.0
D3	1120[b]	− 6.40	3	0.19	149.8	70	Gl (56.1), Ol (4.8), Cpx (34.6), Sp (4.4)	0.51	1.3	4.0
D6	1101[b]	− 6.65	3	0.18	149.8	93	Gl (41.1), Ol (4.4), Cpx (44.0), Pl (5.2), Sp (5.3)	0.40	5.5	6.8
NY17-209										
A1	1201	− 8.40	0	2.35	47.7	18	Gl (96.8), Gl (3.2)	0.59	5.3	13.7
A2	1170	− 8.77	0	2.21	47.8	26	Gl (93.6), Ol (6.4)	0.70	7.4	20.2
A3	1141	− 9.13	0	2.07	47.9	46	Gl, Ol, Cpx, Sp[a]			
A3-5	1119	− 9.41	0	1.97	48	68	Gl, Ol, Cpx, Sp[a]			
A4	1109	− 9.55	0	1.92	48.1	71	Gl (69.7), Ol (7.5), Cpx (21.7), Sp (1.2)	0.60	5.0	13.6
B4	1201	− 6.90	1.5	0.43	49.6	22	Gl (97.2), Ol (2.8)	0.75	10.3	18.3
B5	1169	− 7.28	1.5	0.41	49.6	42	Gl (94.1), Ol (4.9), Sp (0.9)	0.96	3.3	18.2
B1	1139	− 7.66	1.5	0.38	49.6	70	Gl (83.5), Ol (6.4), Cpx (9.8), Sp (0.4)	0.48	9.2	9.9
B2	1118	− 7.93	1.5	0.36	49.6	69	Gl (60.1), Ol (4.7), Cpx (31.7), Sp (3.5)			
B3	1099	− 8.18	1.5	0.34	49.7	94	Gl (44.7), Ol (3.7), Cpx (46.2), Sp (5.3)	0.69	8.1	5.7
D4	1221	− 5.17	3	0.24	149.8	24	Gl (99.2), Sp (0.8)	0.87	1.8	9.9
D5	1201	− 5.40	3	0.23	149.8	23	Gl (98.5), Sp (1.5)	0.79	2.0	7.2
D1	1170	− 5.77	3	0.22	149.8	32	Gl (94.1), Ol (3.7), Cpx (0.3), Sp (1.9)	0.76	5.0	10.6
D2	1140	− 6.14	3	0.20	149.8	65	Gl (55.3), Ol (2.4), Cpx (37.0), Sp (5.3)	0.75	5.4	5.8
D3	1120[b]	− 6.40	3	0.19	149.8	70	Gl (41.4), Ol (3.0), Cpx (51.0), Sp (4.6)	0.97	9.6	15.3
D6	1101[b]	− 6.65	3	0.18	149.8	93	Gl (38.9), Ol (1.0), Cpx (51.9), Sp (8.2)	0.98	2.9	6.2
AZKS003										
G1139	1139	− 10.16	− 1	5.99	44	100	Gl (99.0), Pl (1.0)	0.76	16.9	0.0
G1124	1124	− 10.35	− 1	5.81	44.2	120	Gl (86.6), Ol (3.4), Cpx (0.7), Pl (9.3)	0.50	9.0	1.3
G1109	1109	− 10.55	− 1	5.63	44.4	142	Gl, Ol, Cpx, Pl, Sp[a]			
G1089	1089	− 10.81	− 1	5.35	44.6	161	Gl, Ol, Cpx, Pl, Sp[a], Ilm			
G1071	1071[b]	− 11.06	− 1	5.12	44.9	165	Gl (38.6), Ol (8.6), Cpx (13.4), Pl (36.7), Sp (0.5), Ilm (2.3)	0.82	0.3	11.5

Table 2 (continued)

Run	T (°C)	log fO_2	ΔFMQ	CO (ml/min)	CO2 (ml/min)	Duration (h)	Run products	ΣR^2	Fe-loss [%]	Na-loss [%]
G1050	1050[b]	− 11.36	− 1	4.86	45.1	234	Gl[a], Cpx[a], Pl[a], Sp, Ilm, Wt[a]			
E1168	1168	− 8.73	0	2.20	47.8	47	Gl (100)	0.83	12.1	7.6
E1139	1139	− 9.14	0	2.07	47.9	117	Gl (100)	0.56	12.7	0.9
E1124	1124	− 9.35	0	1.98	48	95	Gl, Ol, Cpx, Pl, Sp[a]			
E1105	1105	− 9.60	0	1.90	48.1	116	Gl (68.8), Ol (5.6), Cpx (5.5), Pl (18.9), Sp (1.2)	0.41	2.1	7.0
E1091	1091	− 9.77	0	1.84	48.2	184	Gl, Ol, Cpx, Pl, Sp[a], Ilm			
E1072	1072	− 10.03	0	1.75	48.2	140	Gl (38.0), Ol (7.1), Cpx (14.1), Pl (37.3), Sp (1.7), Ilm (1.8)	0.59	1.6	11.5
E1050	1050[b]	− 10.36	0	1.65	48.4	166	Gl[a], Cpx[a], Pl, Sp, Wt[a]			
F1171	1171	− 7.26	1.5	0.41	49.6	47	Gl (100)	0.59	9.8	0.7
F1142	1142	− 7.61	1.5	0.38	49.6	93	Gl, Pl, Sp[a]			
F1111-SR	1111	− 8.01	1.5	0.35	49.7	67	Gl (71.4), Ol (3.6), Cpx (5.8), Pl (17.3), Sp (1.9)	0.45	1.4	3.4
F1111	1111	− 8.01	1.5	0.35	49.7	141	Gl (78.7), Ol (3.7), Cpx (3.8), Pl (13.4), Sp (0.4)	0.31	2.8	2.5
F1111-LR	1111	− 8.01	1.5	0.35	49.7	265	Gl (68.9), Ol (4.8), Cpx (5.5), Pl (20.2), Sp (0.6)	0.32	16.9	0.0
F1091	1091	− 8.29	1.5	0.34	49.7	162	Gl (52.8), Ol (4.7), Cpx (11.2), Pl (28.2), Sp (2.8), Ilm (0.1), Psb (0.3)	0.15	5.5	9.5
F1074	1074[b]	− 8.51	1.5	0.32	49.7	188	Gl, Ol, Cpx[a], Pl, Sp			
F1050	1050[b]	− 8.85	1.5	0.30	49.7	238	Gl[a], Cpx[a], Pl[a], Sp, Wt[a]			
H1146	1146	− 6.08	3	0.21	149.8	142	Gl (96.9), Pl (1.8), Sp (1.36)	0.51	1.6	2.3
H1131	1131	− 6.26	3	0.20	149.8	147	Gl (82.4), Cpx (4.5), Pl (10.3), Sp (2.7)	0.42	0.6	2.6
H1095	1095[b]	− 6.72	3	0.18	149.8	216	Gl (47.3), Ol (2.0), Cpx (17.4), Pl (27.5), Sp (4.5), Psb (1.3)	0.23	6.6	15.5
FO22-048										
G1139	1139	− 10.16	− 1	5.99	44	100	Gl (99.8), Ol (0.2)	0.65	11.4	7.4
G1109	1109	− 10.55	− 1	5.63	44.4	142	Gl, Ol, Cpx, Pl, Sp[a]			
G1089	1089	− 10.81	− 1	5.35	44.6	161	Gl (77.4), Ol (3.0), Cpx (14.3), Pl (4.5), Sp (0.74)	0.32	4.8	3.2
G1071	1071[b]	− 11.06	− 1	5.12	44.9	165	Gl (68.8), Ol (2.4), Cpx (22.5), Pl (3.8), Sp (2.5)	0.33	0.8	5.1
G1050	1050[b]	− 11.36	− 1	4.86	45.1	234	Gl, Cpx, Pl[a], Sp, Ilm, Wt[a]			
E1168	1168	− 8.73	0	2.20	47.8	47	Gl (100)	0.66	7.2	13.1
E1139	1139	− 9.14	0	2.07	47.9	117	Gl (100)	0.60	6.8	10.0
E1124	1124	− 9.35	0	1.98	48	95	Gl, Ol, Cpx, Sp[a]	0.52	6.9	3.1
E1105	1105	− 9.60	0	1.90	48.1	116	Gl (85.8), Ol (2.1), Cpx (10.7), Pl (1.0), Sp (0.5)	0.35	1.7	5.0
E1091	1091	− 9.77	0	1.84	48.2	184	Gl (73.3), Ol (2.1), Cpx (20.0), Pl (3.1), Sp (1.6)	0.36	3.6	3.0
E1072	1072	− 10.03	0	1.75	48.2	140	Gl (63.6), Ol (1.2), Cpx (25.7), Pl (5.8), Sp (3.7)	0.35	2.4	9.4
E1050	1050[b]	− 10.36	0	1.65	48.4	166	Gl, Cpx, Pl, Sp, Ilm, Wt[a]			
F1171	1171	− 7.26	1.5	0.41	49.6	47	Gl (99.9), Sp (0.1)	0.55	2.1	0.8
F1142	1142	− 7.61	1.5	0.38	49.6	93	Gl (99.7), Sp (0.3)	0.46	3.7	1.4
F1111-SR	1111	− 8.01	1.5	0.35	49.7	67	Gl (81.0), Cpx (16.5), Sp (2.5)	0.46	0.9	2.7
F1111	1111	− 8.01	1.5	0.35	49.7	141	Gl (79.6), Cpx (18.5), Sp (1.8)	0.59	7.2	1.7
F1111-LR	1111	− 8.01	1.5	0.35	49.7	265	Gl (79.5), Cpx (16.5), Pl (1.2), Sp (2.8)	0.54	2.1	5.2
F1091	1091	− 8.29	1.5	0.34	49.7	162	Gl (67.8), Cpx (27.5), Pl (1.1), Sp (3.6)	0.41	5.5	2.5
F1074	1074[b]	− 8.51	1.5	0.32	49.7	188	Gl (59.6), Cpx (32.1), Pl (3.0), Sp (5.3)	0.44	0.5	8.5
F1050	1050[b]	− 8.85	1.5	0.30	49.7	238	Gl[a], Cpx, Sp, Wt[a]			
H1146	1146	− 6.08	3	0.21	149.8	142	Gl (93.1), Cpx (4.1), Sp (2.8)	0.52	3.8	2.0
H1131	1131	− 6.26	3	0.20	149.8	147	Gl (80.2), Cpx (15.7), Sp (4.1)	0.60	0.8	6.8

Table 2 (continued)

Run	T (°C)	log fO_2	ΔFMQ	CO (ml/min)	CO2 (ml/min)	Duration (h)	Run products	ΣR^2	Fe-loss [%]	Na-loss [%]
H1114	1114	− 6.47	3	0.19	149.8	162	Gl (67.6), Cpx (27.2), Pl (0.4), Sp (4.8)	0.72	0.5	12.1
H1095	1095[b]	− 6.72	3	0.18	149.8	216	Gl (61.6), Cpx (29.4), Pl (3.6), Sp (5.4)	0.44	0.4	20.7
NM19ON009										
G1139	1139	− 10.16	− 1	5.99	44	100	Gl (100)	0.85	20.1	0.4
G1124	1124	− 10.35	− 1	5.81	44.2	120	Gl (95.9), Ol (2.8), Cpx (1.1), Pl (0.2)	0.44	10.8	0.6
G1109	1109	− 10.55	− 1	5.63	44.4	142	Gl, Ol, Cpx, Pl, Sp[a]			
G1089	1089	− 10.81	− 1	5.35	44.6	161	Gl (72.3), Ol (4.5), Cpx (12.9), Pl (9.4), Sp (0.9)	0.37	13.6	0.8
G1071	1071[b]	− 11.06	− 1	5.12	44.9	165	Gl (61.9), Ol (5.0), Cpx (17.6), Pl (13.2), Sp (2.2)	0.76	1.0	8.5
G1050	1050[b]	− 11.36	− 1	4.86	45.1	234	Gl, Ol[a], Cpx, Pl, Sp, Ilm, Wt[a]			
E1168	1168	− 8.73	0	2.20	47.8	47	Gl (100)	0.74	6.4	5.2
E1139	1139	− 9.14	0	2.07	47.9	117	Gl, Ol, Sp[a]			
E1124	1124	− 9.35	0	1.98	48	95	Gl, Ol, Cpx, Pl, Sp[a]			
E1105	1105	− 9.60	0	1.90	48.1	116	Gl (84.4), Ol (4.2), Cpx (6.0), Pl (5.3), Sp (0.2)	0.49	1.7	2.5
E1091	1091	− 9.77	0	1.84	48.2	184	Gl (70.1), Ol (4.8), Cpx (12.4), Pl (11.6), Sp (1.1)	0.42	9.7	8.6
E1072	1072	− 10.03	0	1.75	48.2	140	Gl (64.6), Ol (3.4), Cpx (18.1), Pl (11.0), Sp (2.9)	0.33	1.7	4.2
E1050	1050[b]	− 10.36	0	1.65	48.4	166	Gl, Ol, Cpx, Pl, Sp, Wt[a]			
F1171	1171	− 7.26	1.5	0.41	49.6	47	Gl, Sp[a]			
F1142	1142	− 7.61	1.5	0.38	49.6	93	Gl, Sp[a]			
F1111-SR	1111	− 8.01	1.5	0.35	49.7	67	Gl (81.0), Ol (0.5), Cpx (12.6), Pl (3.4), Sp (2.5)	0.27	5.3	3.8
F1111	1111	− 8.01	1.5	0.35	49.7	141	Gl (84.6), Ol (1.6), Cpx (13.0), Pl (0.5), Sp (0.2)	0.38	11.6	0.7
F1111-LR	1111	− 8.01	1.5	0.35	49.7	265	Gl (82.6), Ol (2.9), Cpx (8.6), Pl (5.4), Sp (0.5)	0.39	14.6	4.5
F1091	1091	− 8.29	1.5	0.34	49.7	162	Gl (65.4), Ol (1.4), Cpx (20.5), Pl (9.0), Sp (3.8)	0.35	6.0	8.2
F1074	1074[b]	− 8.51	1.5	0.32	49.7	188	Gl (56.6), Ol (1.1), Cpx (23.4), Pl (13.0), Sp (5.8)	0.28	2.5	8.6
F1050	1050[b]	− 8.85	1.5	0.30	49.7	238	Gl, Cpx, Sp, Psb[a], Rho[a]			
H1146	1146	− 6.08	3	0.21	149.8	142	Gl (97.7), Cpx (0.7), Sp (1.5)	0.65	9.2	1.6
H1131	1131	− 6.26	3	0.20	149.8	147	Gl (83.3), Cpx (11.9), Pl (1.2), Sp (3.6)	0.46	2.9	4.9
H1114	1114	− 6.47	3	0.19	149.8	162	Gl (71.3), Cpx (16.5), Pl (6.9), Sp (5.3)	0.48	1.5	6.2
H1095	1095[b]	− 6.72	3	0.18	149.8	216	Gl (62.3), Cpx (21.1), Pl (10.3), Sp (6.3)	0.53	0.3	8.4
NY17-219										
G1139	1139	− 10.16	− 1	5.99	44	100	Gl (100)	0.58	7.3	16.2
G1124	1124	− 10.35	− 1	5.81	44.2	120	Gl (99.7), Cpx (0.3)	0.57	10.5	13.5
G1109	1109	− 10.55	− 1	5.63	44.4	142	Gl, Cpx, Sp[a]			
G1089	1089	− 10.81	− 1	5.35	44.6	161	Gl, Ol, Cpx, Sp[a]			
G1071	1071[b]	− 11.06	− 1	5.12	44.9	165	Gl (80.0), Cpx (18.3), Sp (1.8)	0.57	0.5	14.4
G1050	1050[b]	− 11.36	− 1	4.86	45.1	234	Gl, Cpx, Sp, Ne[a]			
E1168	1168	− 8.73	0	2.20	47.8	47	Gl (100)	0.65	9.2	23.3
E1124	1124	− 9.35	0	1.98	48	95	Gl (100)	0.54	3.7	8.7
E1105	1105	− 9.60	0	1.90	48.1	116	Gl (93.5), Cpx (6.5)	0.55	1.7	2.5
E1091	1091	− 9.77	0	1.84	48.2	184	Gl (86.2), Cpx (12.8), Sp (1.0)	0.54	0.6	9.7
E1072	1072	− 10.03	0	1.75	48.2	140	Gl (78.8), Cpx (19.3), Sp (1.9)	0.43	2.9	12.8
E1050	1050[b]	− 10.36	0	1.65	48.4	166	Gl, Cpx, Sp, Ne[a]			
F1171	1171	− 7.26	1.5	0.41	49.6	47	Gl, Sp[a]			
F1142	1142	− 7.61	1.5	0.38	49.6	93	Gl (99.5), Sp (0.5)	0.44	5.4	4.6

Table 2 (continued)

Run	T (°C)	log fO_2	ΔFMQ	CO (ml/min)	CO2 (ml/min)	Duration (h)	Run products	ΣR^2	Fe-loss [%]	Na-loss [%]
F1111-SR	1111	− 8.01	1.5	0.35	49.7	67	Gl (90.5), Cpx (8.0), Sp (1.6)	0.51	0.6	5.3
F1111	1111	− 8.01	1.5	0.35	49.7	141	Gl 86.4), Cpx (12.3), Sp (1.2)	0.38	10.0	7.5
F1111-LR	1111	− 8.01	1.5	0.35	49.7	265	Gl (87.7), Cpx (10.3), Sp (2.0)	0.53	1.1	12.2
F1091	1091	− 8.29	1.5	0.34	49.7	162	Gl (76.0), Cpx (20.8), Sp (3.2)	0.49	0.7	12.2
F1074	1074[b]	− 8.51	1.5	0.32	49.7	188	Gl (70.5), Cpx (25.8), Sp (3.7)	0.53	1.0	16.9
F1050	1050[b]	− 8.85	1.5	0.30	49.7	238	Gl, Cpx, Sp, Wt[a]			
H1146	1146	− 6.08	3	0.21	149.8	142	Gl (98.1), Sp (1.9)	0.51	3.9	6.1
H1131	1131	− 6.26	3	0.20	149.8	147	Gl (90.5), Cpx (6.3), Sp (3.2)	0.46	1.1	5.9
H1114	1114	− 6.47	3	0.19	149.8	162	Gl (79.6), Cpx (16.5), Sp (3.9)	0.45	0.2	11.7
H1095	1095[b]	− 6.72	3	0.18	149.8	216	Gl (70.7), Cpx (24.7), Sp (4.6)	0.53	0.0	28.6

Mass-balance calculations are missing for some samples due to at least one phase being too small for reliable EPMA measurements

Gl glass, *Sp* spinel, *Ol* olivine, *Cpx* clinopyroxene, *Pl* plagioclase, *Ilm* ilmenite, *Psb* pseudobrookite, *Wt* whitlockite, *Rho* rhönite, *Ne* nepheline

[a]Phase too small for reliable EPMA measurement

[b]Thermal oscillations of + 10 °C above the target temperature were applied for the first 10 h of the experiment

111312-44), Plagioclase (NMNH 115900), Kakanui augite (NMNH 122142), Ilmenite (NMNH 96189), Magnetite (NMNH 114887) and Chromite (NMNH 117075) (Jarosewich et al. 1980) and MongOL Sh11-2 (Batanova et al. 2019). Major element accuracies (determined using reference materials) are typically <2%; 1σ precisions, determined from repeat measurements of reference materials, are reported in Table S1 (Supplementary Material 3).

Numerous algorithms are available for calculating iron speciation in melts (e.g. Kress and Carmichael 1991; Putirka 2016; Borisov et al. 2018; Sun and Yao 2024). Each model is based on a different calibration dataset, with some better suited for certain compositions over others. Throughout this study, we chose to use the algorithm of Kress and Carmichael (1991) to aid comparisons with other works where it is commonly used. Nonetheless, we evaluate the effect of this choice (e.g. on mineral-melt Fe–Mg exchange) in Supplementary Material 2.

The proportions of Fe^{2+} and Fe^{3+} were determined stoichiometrically in clinopyroxene, spinel, ilmenite and pseudobrookite, using the method of Droop (1987), as recommended by Neave et al. (2024a, b). Due to small sizes and zoning features in clinopyroxene (see below) which have affected EPMA analyses, all clinopyroxene EPMA measurements were evaluated for multicomponent equilibrium with the melt, using the equations of Putirka (1999) for the CaTs ($CaAlAlSiO_6$) component and Mollo et al. (2013) for the DiHd ($Ca(Mg,Fe^{2+})Si_2O_6$) and EnFs ($(Mg, Fe^{2+})_2Si_2O_6$) components respectively that treat all Fe as Fe^{2+}. We subsequently recalculated clinopyroxene components using the scheme of Neave et al. (2024a, b) that accounts for the presence of Fe^{3+}. Clinopyroxene nomenclature follows the quadrilateral scheme of Morimoto (1988).

Oxide phases produced along the ilmenite–haematite ($Fe^{2+}TiO_3$–$Fe^{3+}{}_2O_3$)—pseudobrookite–ferropseudobrookite ($Fe^{3+}{}_2TiO_5$–$Fe^{2+}Ti_2O_5$) solid solution were calculated using the method of Andersen et al. (1993). Olivine Fo content was calculated as molar [100·Mg/(Mg + Fe_{tot})], while plagioclase An content was calculated as molar [100·Ca/(Ca + Na)]. Clinopyroxene Mg# was calculated as molar [100·Mg/(Mg + Fe^{2+})].

Attainment of equilibrium

Experimental equilibrium was determined based on compositional and textural characteristics. Crystals are generally euhedral, and show no compositional zonation (Figs. 4 and 5). However, clinopyroxenes show compositional variability as a result of sector zoning (e.g., Kouchi et al. 1983; Neave et al. 2019). Experimental glasses are also homogenous, and along with mineral phases, generally display systematic compositional trends with changes in experimental conditions. Minor variability in phase compositions in some experiments is attributed to mixed analyses.

A few of the evolved experiments at the lowest temperatures showed some signs of disequilibrium (bimodal glass compositions, phase compositions not in line with compositional trend). These experiments are excluded from discussion of compositional trends but were retained in Table 2 and in phase diagrams (Fig. 2) to provide insights into mineral saturation temperatures, albeit with caveats.

Our run durations ranged between 18–238 h and were comparable to those used in similar previous studies (Mahood and Baker 1986; Thy and Lofgren 1994). We additionally performed a time series at 1111 °C and FMQ + 1.5 with durations of 67, 141 and 265 h to assess the effect on the phase assemblage and compositions. All experiments

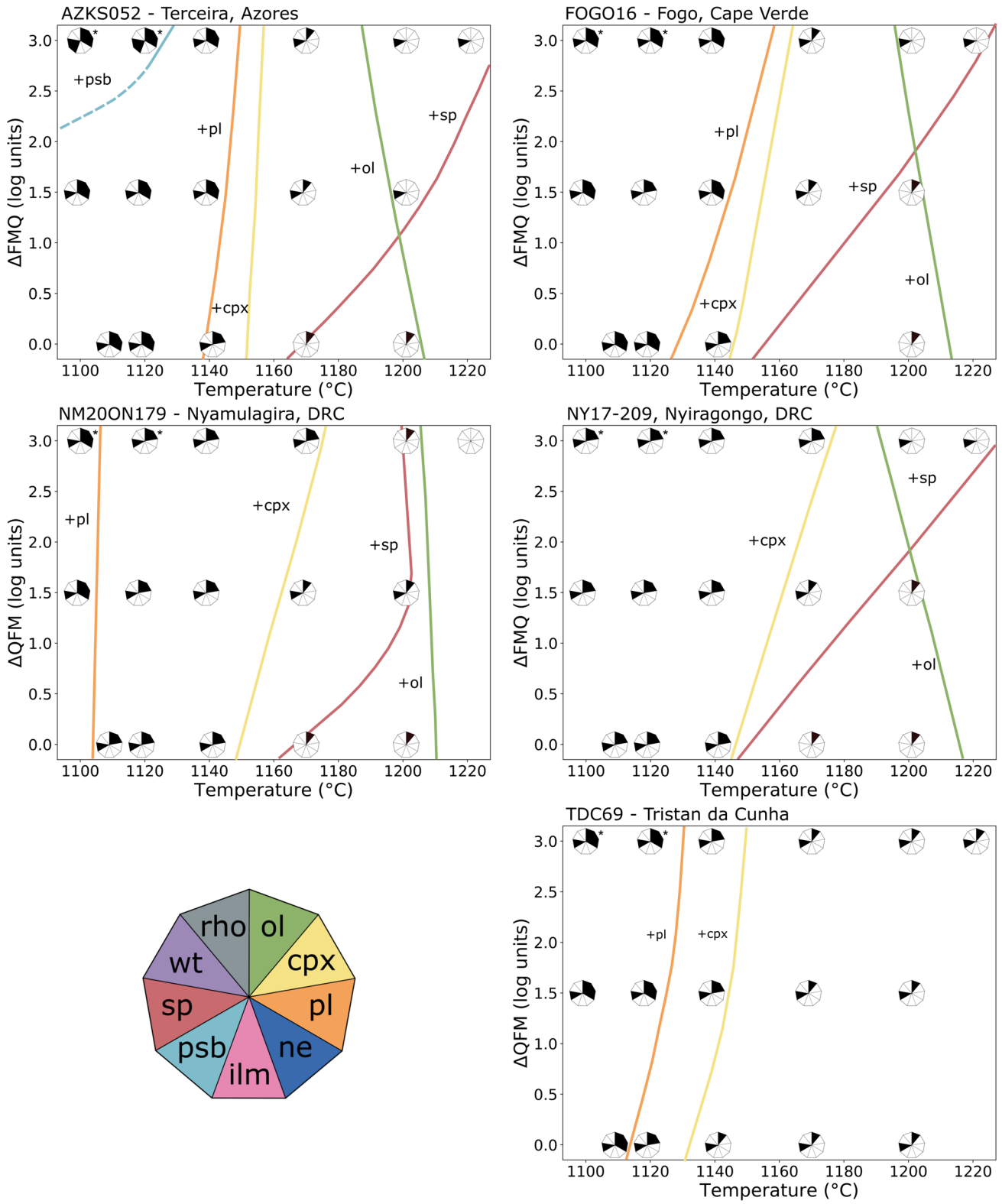

Fig. 2 Phase relations of the primitive compositions as a function of temperature and fO_2. *sp* spinel, *ol* olivine, *cpx* clinopyroxene, *pl* plagioclase, *ilm* ilmenite, *psb* pseudobrookite, *wt* whitlockite, *rho* rhönite, *ne* nepheline. Some phases listed are only present in experiments on evolved compositions. Filled segments in each marker reflect presence of the corresponding phase shown in the legend. Continuous lines mark the onset of crystallisation of a given phase. Dotted line indicates continuation of the phase boundary which has limited experimental constraints. Stars indicate experiments in which thermal oscillations were applied

were found to have identical phase assemblages, with the exception of the long run for composition FO22-048, which produced additional plagioclase. This is likely due to a slight difference in the position of the experimental charge within the hotspot. Repeat experiments were also texturally and compositionally similar, suggesting that chosen run durations were sufficient to approach equilibrium. For most compositions, Na-loss, calculated via mass-balance (see below), was highest for experiments with run durations of 265 h, however in only one composition, NY17-219, did Na-loss increase monotonically with temperature.

Estimation of phase proportions

Modal phase proportions were estimated using a non-negative least squares algorithm implemented in python [https://github.com/eazzzon/MassBalanceCal] by Zhang et al. (2023) and are reported in Table 2. The sum of residual squares (ΣR^2) was < 1 for all experiments. Iron- and Na-loss were calculated by including a pure FeO phase and a pure Na_2O phase in the calculations. Experiments with significant apparent Na-loss, in particular those at low temperatures, are likely to be due to the challenges associated with measuring small glass pools. These experiments often have small residual melt pools (< 10 µm), leading to alkali migration during measurement with reduced beam diameters, or may only have melt pools at the edge of the experimental charge, where Na-loss is greatest, due to evaporation in the furnace at the liquid–gas interface (Tormey et al. 1987). These factors may lead to overestimation of Na-loss, and thus reported values should be treated as maximum values.

Results

Phase relations

The equilibrium phase relationships for primitive and evolved experiments are illustrated as temperature (T)-fO_2 diagrams in Figs. 2 and 3 and listed in Table 2.

Primitive compositions

At FMQ, olivine is the liquidus phase across all compositions, followed by spinel, clinopyroxene ± plagioclase (Fig. 2). Composition NY17-209, the most silica-undersaturated, is never observed to produce plagioclase. The stability of Fe bearing minerals such as olivine and spinel is most heavily affected by changes in fO_2. With the exception of sample TDC69, where saturation temperatures are undefined (i.e. higher than our highest experimental temperature), olivine saturation temperatures decrease from ~ 1200–1220 °C to ~ 1170–1200 °C as fO_2 increases from FMQ to FMQ + 3. Olivine is replaced by spinel as the first liquidus phase under oxidising conditions, except for sample NM20ON179, crystallizing at ~ 1141–1170 °C at FMQ and above 1200 °C at FMQ + 3. Clinopyroxene and plagioclase (where observed) show very similar saturation curves, with both phases showing only minor increases in saturation temperature with increasing fO_2. Sample AZKS052 additionally crystallises pseudobrookite at 1120–1100 °C at FMQ + 3.

Evolved compositions

In contrast with the primitive series of experiments, phase relations and crystallisation temperatures in the evolved series are much less consistent between compositions but still show some common trends. Under oxidising conditions (FMQ + 1.5 and FMQ + 3), spinel is the liquidus phase, saturating above 1171 °C in all samples except AZKS003, which saturates spinel between 1142 °C and 1171 °C at FMQ + 1.5. Similarly to the primitive experiments, the saturation temperature of spinel falls with decreasing fO_2, crystallizing between 1109 °C and 1124 °C (AZKS003, FO22-048, NM19ON009) or between 1071 °C and 1089 °C (NY17-219) at FMQ-1. Under these reducing conditions, the liquidus phase varies between olivine (FO22-048, NM19ON009), clinopyroxene (NY17-219) or plagioclase (AZKS003) with starting composition. Olivine saturation temperatures range from 1120 °C to above 1139 °C at FMQ-1, except for NY17-219 in which olivine crystallises at 1089–1109 °C. Saturation temperatures fall with increasing fO_2, though the stability of olivine also depends heavily on starting composition. In compositions with the highest alkali and CaO contents (FO22-048 and NY17-219), olivine is absent from the assemblage at higher fO_2. Compositions with more SiO_2 and less CaO (NM19ON009, AZKS003) produce olivine between 1111–1142 °C at FMQ + 1.5, with olivine being found at 1095 °C at FMQ + 3 in AZKS003 (Fig. 5d), the composition with the lowest alkali content.

Clinopyroxene stability is weakly dependent on fO_2, with clinopyroxene crystallizing between 1109–1140 °C at FMQ-1 and at temperatures ~ 10–15 °C higher at FMQ + 3. Plagioclase saturation varies little with fO_2, but does vary with starting composition. Sample AZKS003 saturates in plagioclase at ~ 1140 °C, while the more silica-undersaturated compositions NM19ON009 and FO22-048 produce plagioclase at ~ 1130–1140 °C and ~ 1110–1120 °C respectively. The most silica-undersaturated sample, NY17-219, does not produce plagioclase, though nepheline is present in the lowest temperature runs at FMQ and FMQ-1 (Fig. 5c). Ilmenite is produced under all but the most oxidising conditions for AZKS003, at ~ 1090–1110 °C. However, it is

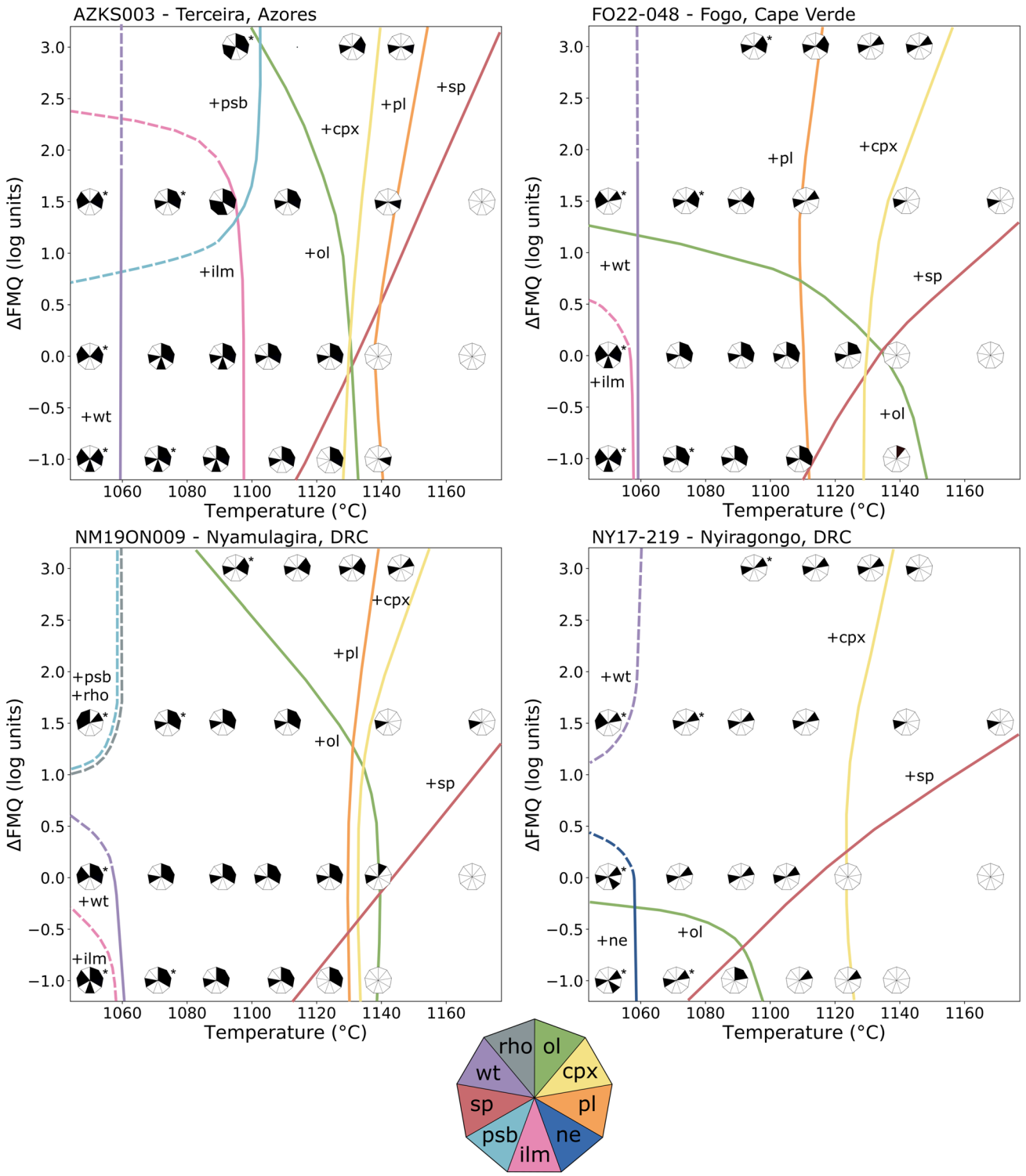

Fig. 3 Phase relations of the evolved compositions as a function of temperature and fO_2. Legend is the same as for Fig. 2

only present at 1050 °C for FO22-048 and NM19ON009 at FMQ-1 to FMQ and FMQ, respectively. Pseudobrookite is produced from AZKS003 (Fig. 5d) and NM19ON009 under oxidising conditions, crystallizing at ~1090–1110 °C in the former, at FMQ+1.5 and FMQ+3, but only at 1050 °C at FMQ+1.5 in the latter. Rhönite is also observed in NM19ON009 under the same conditions. Whitlockite saturates in all samples between 1050–1070 °C. Samples AZKS003 and FO22-048 produce whitlockite at all fO_2

conditions, but NM19ON009 and NY17-219 only produce it at FMQ and FMQ-1, and FMQ + 1.5 respectively.

Phase chemistry and textures

Olivine

Olivine crystals in both primitive and evolved experiments are typically euhedral, and often contain rounded or elongate inclusions of glass (Figs. 4d, e, 5a, f). Crystal size decreases with temperature, with the largest crystals formed close to the liquidus. While most crystals are euhedral, some have rounded shapes (Fig. 4e), possibly a result of extensive initial crystallisation and subsequent partial resorption as experimental charges equilibrate (Berndt et al. 2005; Marxer et al. 2022). Solid inclusions are common, typically of spinel at higher temperatures, while lower temperature olivine crystals may contain numerous different phases, likely as a result of rapid nucleation of different co-crystallising phases (Marxer and Ulmer 2019).

Olivine compositions are shown with respect to temperature and fO_2 in Fig. 6. Primitive olivine forsterite contents range from Fo_{74} to Fo_{93}, while evolved olivines are in the range Fo_{60} to Fo_{85}. At a given temperature, olivine Fo content increases as a function of fO_2, due to the higher $Fe^{3+}/\Sigma Fe$ content of equilibrium melts. This increase is most pronounced between the highest fO_2 conditions due to the non-linear relationship between fO_2 and melt $Fe^{3+}/\Sigma Fe$ (Kress and Carmichael 1991; Feig et al. 2010), where the curve has a sigmoidal form. Forsterite content falls as temperature decreases, however the extent to which this occurs depends primarily on prevailing fO_2 conditions, as well as melt composition. Under the most oxidising conditions, extensive crystallisation of magnetite-rich spinel lowers FeO_{tot} concentrations in the melt, and combined with high melt $Fe^{3+}/\Sigma Fe$ produces consistently high-forsterite olivines.

Plagioclase

Plagioclase is characterised by large, euhedral, lath-shaped crystals, commonly bearing inclusions of spinel and clinopyroxene. Crystals may be up to 400 µm in length and 50 µm in width (Fig. 5a, f), with plagioclase in experiments on evolved compositions typically larger than those in their primitive counterparts. Plagioclase laths decrease in size as experimental temperatures fall, with crystals < 3 µm in width found at the lowest temperatures (Fig. 4a vs b). They additionally acquire a more irregular, anhedral form in some compositions (Figs. 4d, 5d), appearing as fragmented laths. A similar effect is observed as fO_2 is increased (Fig. 5a, b), where crystals decrease in size, and are filled with significantly more inclusions, which in some cases inhibit accurate measurement of phase composition. Similarly to olivine, this may be the result of rapid nucleation of different co-crystallising phases (Marxer and Ulmer 2019).

Plagioclase compositions are shown as a function of temperature and fO_2 in Fig. 7. The anorthite content of primitive plagioclase varies between An_{81} and An_{55}, while that of evolved plagioclase varies between An_{71} and An_{27}. Anorthite content decreases continuously with falling temperatures for all starting compositions and redox conditions. Anorthite content additionally decreases slightly at a given temperature as prevailing fO_2 conditions become more oxidising, an indirect effect of increased crystal fractions of clinopyroxene at higher fO_2. In line with previous experiments (Toplis and Carroll 1995; Feig et al. 2010; Mollo et al. 2011; Salazar-Naranjo and Vlach 2023), plagioclase Fe contents increase with increasing fO_2.

The Ca-Na distribution coefficient between plagioclase and melt, $K_{D_{Ca-Na}}^{Pl-Melt}$, is dependent on both temperature and composition (e.g. Hamada and Fujii 2007; Honma 2012; Namur et al. 2012). We observe strong positive correlations between $K_{D_{Ca-Na}}^{Pl-Melt}$ and melt Al_2O_3/SiO_2, matching the observations of an alkali basalt of Honma (2012), and negative correlations between $K_{D_{Ca-Na}}^{Pl-Melt}$ and melt Ca# (= Ca/Ca + Na). Composition FO22-048, whose melt has the highest Al_2O_3/SiO_2, records plagioclase $K_{D_{Ca-Na}}^{Pl-Melt}$ values between 2.25–3.19. Comparatively, AZKS052, whose melt has the lowest Al_2O_3/SiO_2, records the lowest (0.84–1.22).

Clinopyroxene

Clinopyroxene occurs as small, euhedral crystals, which vary from prismatic to equant depending on starting composition. Crystals are typically < 10 µm, with those at the lowest temperatures < 5 µm. Starting composition AZKS003 proved an exception, producing very large clinopyroxene crystals, up to 150 µm in length. Clinopyroxene crystals were present in experiments at all fO_2 conditions, providing the melt fraction was high and experimental temperatures were close to the clinopyroxene liquidus (between 1105–1124 °C).

The nature of clinopyroxene zoning depends strongly on the composition of the starting material, with many crystals displaying sector zoning. In our experiments, well developed sector zones could be observed even at the lowest temperature (Fig. 5c). We find that hourglass sectors are enriched in SiO_2 and MgO, while prism sectors are enriched in Al_2O_3, TiO_2 and FeO. Based on published experimental studies (e.g., Marxer et al. 2022; Neave et al. 2019; Zhang et al. 2023), we interpret sector zoning, observed to various degrees, as a feature typically explained by near-equilibrium

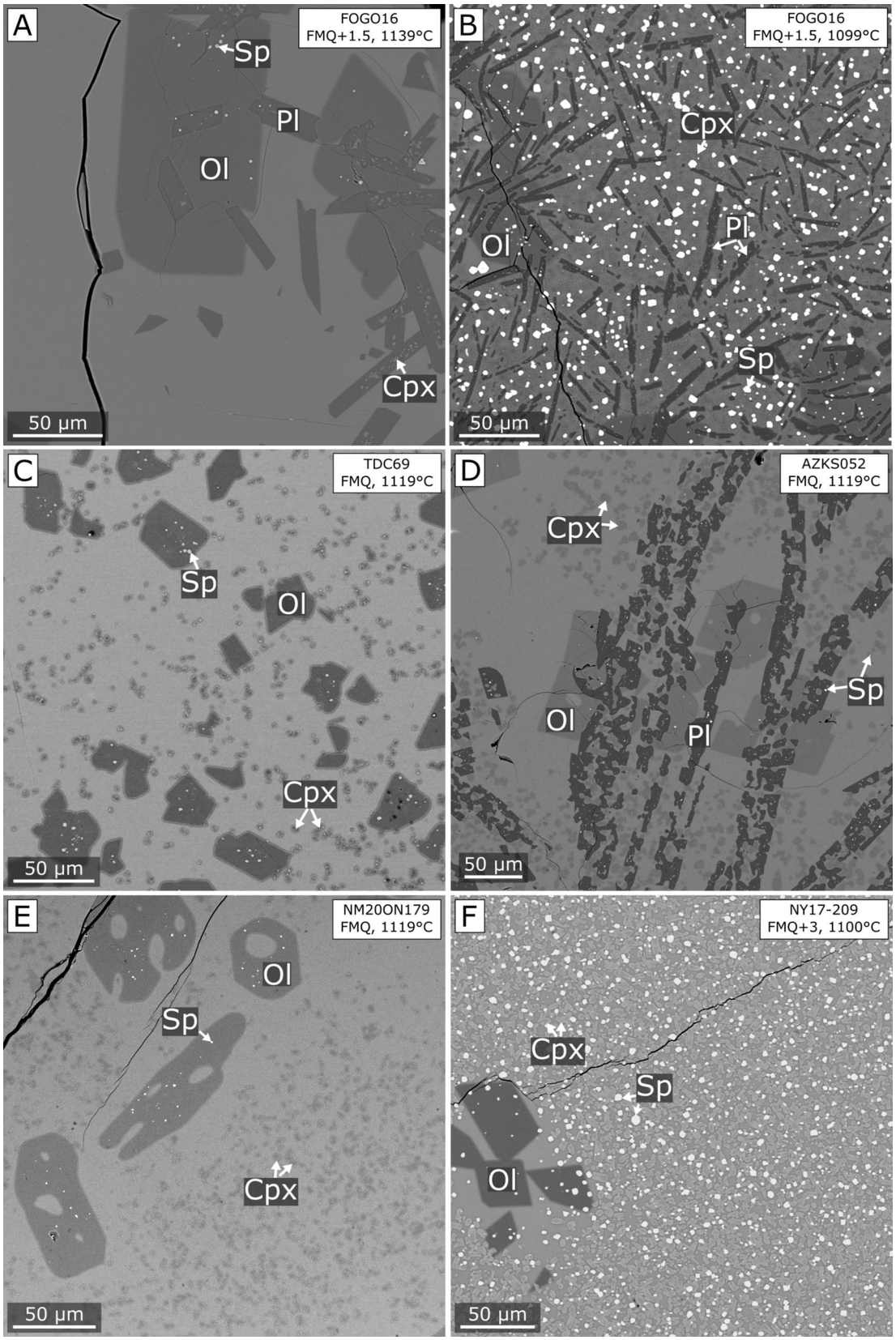
A
FOGO16
FMQ+1.5, 1139°C
Sp
Pl
Ol
Cpx
50 µm
B
FOGO16
FMQ+1.5, 1099°C
Cpx
Pl
Ol
Sp
50 µm
C
TDC69
FMQ, 1119°C
Sp
Ol
Cpx
50 µm
D
AZKS052
FMQ, 1119°C
Cpx
Sp
Ol
Pl
50 µm
E
NM20ON179
FMQ, 1119°C
Ol
Sp
Cpx
50 µm
F
NY17-209
FMQ+3, 1100°C
Cpx
Sp
Ol
50 µm

Fig. 4 Backscattered electron (BSE) images of run products obtained in experiments using primitive compositions. *Ol* olivine, *Sp* spinel, *Cpx* clinopyroxene, *Pl* plagioclase. **A** FOGO16 (FMQ+1.5, 1139 °C) Large euhedral olivine with included plagioclase laths containing clinopyroxene and spinel inclusions; **B** FOGO16 (FMQ+1.5, 1099 °C) Similar to A, with much smaller grain size, and higher crystal fraction of clinopyroxene and spinel, present throughout; **C** TDC69 (FMQ, 1119 °C) euhedral olivine containing spinel inclusions, with small clinopyroxene; **D** AZKS052 (FMQ, 1119 °C) large euhedral olivine with disjointed chains of plagioclase containing small spinel inclusions, and clinopyroxene; **E** NM20ON179 (FMQ, 1119 °C) rounded olivines (compared with those in **C** and **D**) containing spinel and glass inclusions, and clinopyroxene; **F** NY17-209 (FMQ+3, 1100 °C) assemblage dominated by clinopyroxene along with spinel. Euhedral olivine is surrounded by glass

crystallisation at relatively low degrees of undercooling ($\Delta T = T_{cpx\text{-}liquidus} - T_{experiment}$) (Kouchi et al. 1983; Ubide et al. 2019; Masotta et al. 2020). A value of $\Delta T < 45$ °C is considered the threshold for the formation of sector-zoning (Masotta et al. 2020), however we continue to observe this feature even at $\Delta T \geq 74$ °C. This observation may be attributed to the isothermal nature of our experiments compared with those of Masotta et al. (2020) which were performed with defined cooling rates.

On occasion, clinopyroxenes, especially those produced from sample AZKS003, contained subhedral to anhedral patchy cores of Al-rich clinopyroxene (Fig. 5d). These cores, present at all fO_2 conditions and over a wide array of temperatures, are typically distinguished by their irregular nature, with no consistent form observed between grains. These cores were unavoidable during analyses in some cases due to the small size of the crystals (Fig. 5d), or else difficult to distinguish from true Al-rich sectors in others. Similar features in previous experimental works, have been described as metastable cores formed during nucleation (Marxer et al. 2022), or skeletons of pyroxenes formed through rapid growth at high initial undercooling, later infilled or overgrown by Al-poor pyroxene (Pontesilli et al. 2019; Masotta et al. 2020; MacDonald et al. 2023).

Clinopyroxenes from experiments on both primitive and evolved compositions fall in the diopside and augite fields of the clinopyroxene quadrilateral of Morimoto (1988), although many plot above the diopside–hedenbergite (Di-Hd) tie line, a consequence of containing high proportions of non-quadrilateral components. Clinopyroxene Mg# (100 $Mg/(Mg+Fe^{2+})$) ranges between 81–97 for primitive compositions and 73–97 for evolved compositions and correlates positively with both fO_2 (Fig. 8) and temperature (Fig. S4, Supplementary Material 2). Clinopyroxenes produced from the primitive composition NY17-209 however, show negative correlation between Mg# and temperature, which reflects the Mg# of the melt (when calculated as 100 $Mg/Mg+Fe^{2+}$), which remains high due to the high melt $Fe^{3+}/\sum Fe$. The partition coefficient $D_{Fe^{3+}}^{cpx-melt}$ ranges from 0.67–2.67 for primitive compositions, and from 0.93–5.78 for evolved compositions.

All clinopyroxenes become progressively depleted in the DiHd component with increasing fO_2 (Fig. 8). The ^{VI}Al-poor (primitive: FMQ, 0–0.09 apfu; FMQ+3, 0–0.05 apfu; and evolved: FMQ-1, 0–0.11 apfu; FMQ+3, 0–0.08 apfu) nature of clinopyroxene in our experiments, results in ^{IV}Al—thought to mediate the incorporation of Fe^{3+} cations in clinopyroxene (Neave et al. 2024a, b)—predominantly forming the esseneite (Ess, $CaFe^{3+}AlSiO_6$) component (Fig. 8). The stability of esseneite is enhanced at high fO_2 (Conte et al. 2009) and is positively correlated with temperature (Fig. S4, Supplementary Material 2). In addition, ^{IV}Al is used to form the titanium pyroxene (CaTi, $CaTiAl_2O_6$) (Fig. 8) component, whose concentration falls with temperature, as well as forming Na-bearing components. The ^{IV}Al bearing calcium-Tschermak (CaTs, $CaAlAlSiO_6$) component however, is only present in small quantities (≤ 0.03 apfu) at FMQ-1 and FMQ, if present at all.

Sodium is incorporated as both aegirine (Ae, $NaFe^{3+}Si_2O_6$) and jadeite (Jd, $NaAlSi_2O_6$) components. Clinopyroxene Na_2O contents are correlated with melt alkalinity index (=molar $(Na_2O+K_2O)/Al_2O_3$) (Fig. S5, Supplementary Material 2), with the most alkaline starting compositions (NY17-209 and NY17-219) typically producing Na_2O rich clinopyroxene, up to 0.6 wt% and 1.0 wt% respectively. Increasing fO_2 and decreasing temperature promotes melt Na_2O enrichment in both the melt (see below) and in clinopyroxene, where it is dominantly incorporated via Ae under the most oxidising conditions.

Spinel and Fe-Ti oxides

Several spinel supergroup minerals are found in our experiments and are classified according to the method of Bosi et al. (2019). These spinels (sensu lato, s.l.) are present as subhedral to euhedral, equant crystals, < 10 µm in size (Figs. 4, 5), and are often seen as inclusions in other phases, pointing to early initial crystallisation.

Spinel s.l. are most commonly magnetite ($Fe^{2+}Fe^{3+}{}_2O_4$), or magnesioferrite ($Mg^{2+}Fe^{3+}{}_2O_4$) in experiments on primitive compositions. Run D4 (1221 °C, FMQ+3; AZKS052) and run B5 (1169 °C, FMQ+1.5; FOGO16) produced spinel (sensu stricto) ($Mg^{2+}Al^{3+}{}_2O_4$), while hercynite ($Fe^{2+}Al^{3+}{}_2O_4$) was present in composition TDC69 in run A3-5 (1119 °C FMQ). Magnesioferrite is most stable under oxidising conditions and is absent from all experiments at FMQ. With both decreasing temperature and fO_2, magnesioferrite is replaced by magnetite. Spinel s.l. in experiments on evolved compositions are classified as either magnetite or ulvöspinel ($Fe^{2+}{}_2Ti^{4+}O_4$), with the latter restricted to experiments at FMQ and FMQ-1.

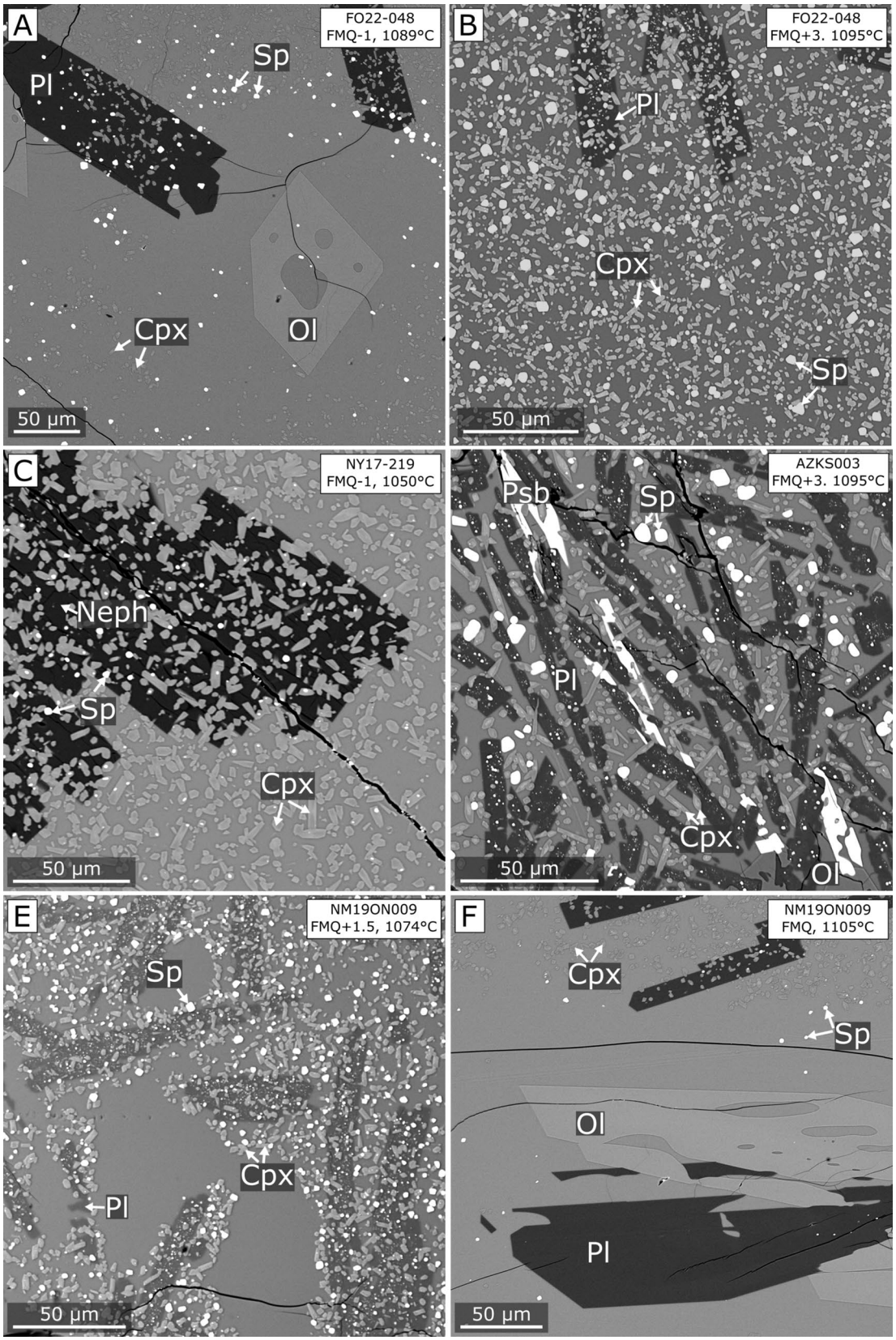
A
FO22-048
FMQ-1, 1089°C
Sp
Pl
Cpx
Ol
50 µm
B
FO22-048
FMQ+3. 1095°C
Pl
Cpx
Sp
50 µm
C
NY17-219
FMQ-1, 1050°C
Neph
Sp
Cpx
50 µm
AZKS003
FMQ+3. 1095°C
Psb
Sp
Pl
Cpx
Ol
50 µm
E
NM19ON009
FMQ+1.5, 1074°C
Sp
Cpx
Pl
50 µm
F
NM19ON009
FMQ, 1105°C
Cpx
Sp
Ol
Pl
50 µm

Fig. 5 BSE images of run products obtained in experiments using evolved compositions. *Ol* olivine, *Sp* spinel, *Cpx* clinopyroxene, *Pl* plagioclase, *Psb* pseudobrookite, *Neph* nepheline. **A** FO22-048 (FMQ-1, 1089 °C) large euhedral olivine containing rounded glass inclusions and large euhedral plagioclase, with small clinopyroxene and spinel crystals, often included in plagioclase; **B** FO22-048 (FMQ+3, 1095 °C) at higher fO_2 grain size is smaller, olivine is absent, and spinel and clinopyroxene are ubiquitous; **C** NY17-219 (FMQ-1, 1050 °C) large euhedral nepheline included with sector zoned clinopyroxene; **D** AZKS003 (FMQ+3, 1095 °C) elongate disjoined plagioclase with small spinel inclusions, euhedral olivine, clinopyroxenes containing patchy Al-rich cores, spinel and pseudobrookite; **E** NM19ON009 (FMQ+1.5, 1074 °C) euhedral plagioclase laths, clinopyroxene and spinel, with the latter two often included in plagioclase. Pockets of melt found between areas of higher crystallinity; **F** NM19ON009 (FMQ, 1095 °C) very large, euhedral olivine with elongate glass inclusions, euhedral plagioclase with some smaller grains containing included clinopyroxene and spinel

Figure 9 shows the main compositional trends observed in spinel supergroup minerals. Spinel s.l. composition is highly dependent on temperature in addition to fO_2, with Fe^{3+}# (i.e., $Fe^{3+}/Fe^{3+}+Al^{3+}$) and Fe^{2+}# (i.e., $Fe^{2+}/Fe^{2+}+Mg^{2+}$) increasing systematically as temperature falls (Fig. 9a). As fO_2 increases from FMQ-1 to FMQ+3, spinel s.l. compositions are shifted to lower Fe^{2+}# and higher Fe^{3+}#. TiO_2 content is also coupled with Fe^{2+}# (Fig. 9b), stabilising ulvöspinel at low temperatures and fO_2 conditions.

Spinels s.l. with significant Cr_2O_3 contents, up to 24.7 wt% and 11.1 wt% in primitive and evolved experiments respectively, are found only in high temperature experiments from each series. Moreover, Cr_2O_3 contents fall with temperature, with the onset of clinopyroxene crystallisation typically coinciding with the disappearance of Cr_2O_3 (< 1 wt%) from spinel s.l. compositions, as also observed by Feig et al. (2010).

Other oxide phases produced in these experiments are ilmenite ($Fe^{2+}TiO_3$) and pseudobrookite ($Fe^{3+}{}_2TiO_5$). Ilmenite, present in evolved experiments, is typically euhedral and elongate, up to ~10 µm in length, but may also appear as equant, blocky crystals. Ilmenite composition is correlated with both fO_2 and temperature. X_{ilm} decreases with temperature, and with increasing fO_2, with X_{ilm} falling from $X_{ilm}=0.95$ to $X_{ilm}=0.79$ between FMQ-1 and FMQ+1.5.

Pseudobrookite, present at FMQ≥1.5, forms chains of subhedral, elongate crystals up to 15 µm in length in primitive samples but takes on a more euhedral shape in experiments on evolved compositions, up to 30 µm in length (Fig. 5d). Experiments on primitive compositions have pseudobrookite with $X_{Psb}=0.68$–0.72. In experiments on evolved compositions, $X_{Psb}=0.47$–0.64, increasing by 0.17 between FMQ+1.5 and FMQ+3, a result of increasing Fe^{3+} content in the melt. Primitive pseudobrookites are slightly richer in Al_2O_3, with 2.1–2.4 wt%, compared with 1.6–1.8 wt% in evolved pseudobrookite. MgO content falls in a similar range for both primitive and evolved, with 5.9–6.1 wt% MgO.

Glass

Glasses cover a wide range of compositions (Fig. 10), with their evolutionary paths controlled by the types and proportions of crystallising mineral phases. They range from basaltic and basanitic to trachyandesitic (compositions AZKS052, AZKS003, FOGO16 and TDC69), basanitic to tephriphonolitic (compositions NM20ON179, NM19ON009, FO22-048 and NY17-219), and from basanitic to nephelinitic (composition NY17-209), classified according to the fields defined by Le Bas et al. (1986) on the TAS diagram (Fig. 11a, c). The compositional evolution of glasses is shown as a function of decreasing temperature in Figs. S6–S9 (Supplementary Material 2), and as a function of MgO content in Fig. 10. In general, we see broadly similar compositional trends in those samples that produce similar crystallizing assemblages (e.g. primitive samples NY17-209, NM20ON179 and TDC69 and evolved samples NY17-219 and FO22-048).

We notice that, in addition to the bulk starting composition (see above), two parameters play key roles in controlling melt composition evolution: temperature and fO_2. Across all samples and redox conditions, MgO contents decrease continuously with decreasing temperature. Similarly, CaO concentrations fall with temperature, albeit preceded by an initial phase of slightly increasing CaO in primitive samples (Fig. 10a, c, e, g), as long as clinopyroxene is not on the liquidus. The most calcic starting composition, primitive sample NY17-209 reaches 16.8 wt% CaO before falling, while sample AZKS052, the least calcic primitive composition reaches only 12.1 wt% CaO. This inflection point coincides with the saturation of clinopyroxene. The extent to which CaO contents fall, after clinopyroxene saturation, increases as fO_2 conditions become more oxidising.

With decreasing temperature, residual melts become increasingly enriched in incompatible elements. This is illustrated by Na_2O and K_2O both increasing as temperature falls (Figs. S6–S9, Supplementary Material 2). Note, however, that Na_2O remains approximately constant at around 4–4.5 wt% in evolved sample AZKS003, reflecting the lower anorthite content of plagioclase crystallised by this composition. In some evolved compositions, Na_2O appears to fall at the lowest temperatures, though this is likely an artefact from alkali migration during measurement with smaller beam sizes (see above). P_2O_5 follows similar trends to the alkalis, rising in primitive and evolved samples alike, before the saturation of whitlockite at 1050 °C, at which point concentrations are either maintained or fall.

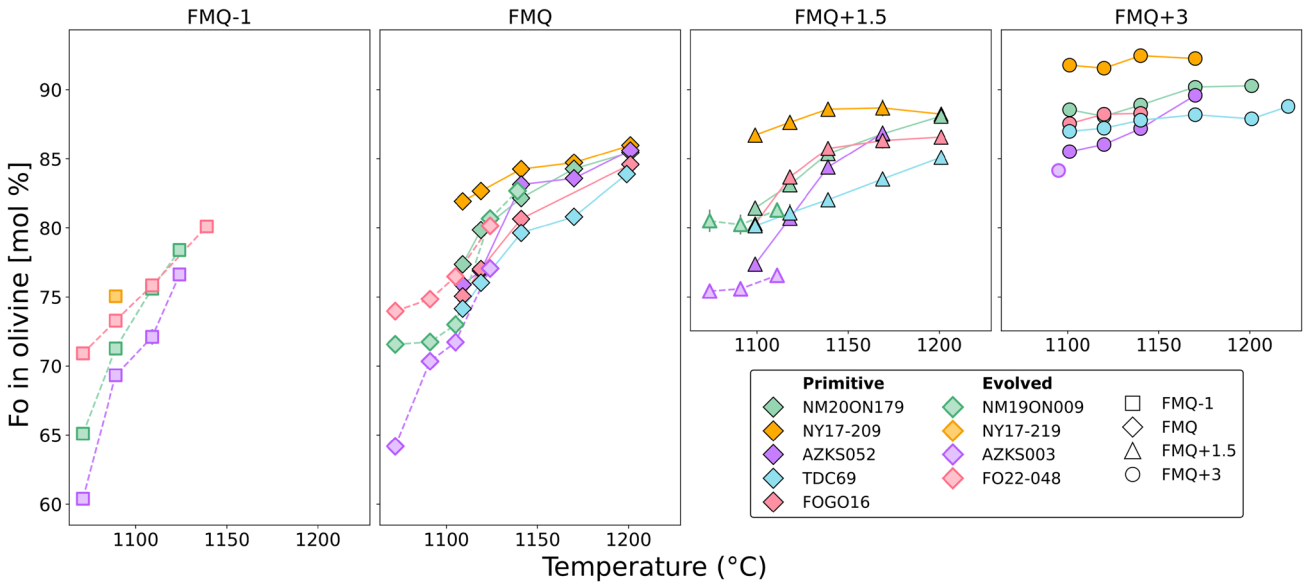

Fig. 6 Olivine forsterite content at a given fO_2 as a function of temperature, for olivines found in experiments using primitive (symbols with black outlines) and evolved starting compositions (symbols with coloured outlines)

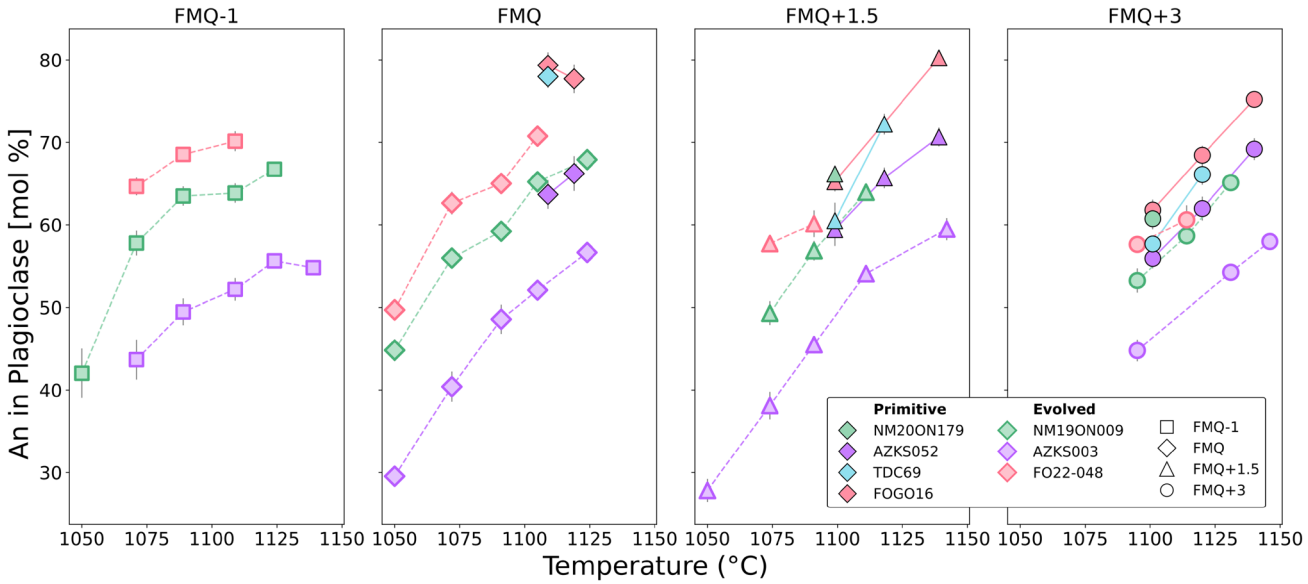

Fig. 7 Plagioclase anorthite content at a given fO_2 as a function of temperature, for plagioclase found in experiments using primitive (symbols with black outlines) and evolved starting compositions (symbols with coloured outlines)

Some melts show bi-modal compositions at the lowest temperatures in the evolved series. Specifically, we observe that conjugate high-silica melts are enriched in Al_2O_3, Na_2O and K_2O, and depleted in TiO_2, FeO, MgO, CaO and P_2O_5 relative to their low-silica counterparts. This may be the result of poor equilibration of these particular samples, with melts reflecting the nearest crystallizing phases, i.e. the development of a compositional boundary layer in highly-polymerized melts. Alternatively, elemental partitioning indicates that we may be observing the initiation of silicate immiscibility (Charlier and Grove 2012; Charlier et al. 2013), although the paired immiscible melts are not clearly separated in our experiments. Such potential diffuse immiscibility has been reported in previous studies (e.g. Longhi 1990; Charlier and Grove 2012; Honour et al. 2019) but the compositional field for the onset of immiscibility along the evolution of alkali basalts remains to be investigated at temperature < 1050 °C.

Prevailing fO_2 conditions influence the evolution of many elements, and SiO_2, FeO and TiO_2 in particular, are mainly controlled by the crystallisation of spinel and Fe-Ti oxides. In all experiments, excluding evolved experiments

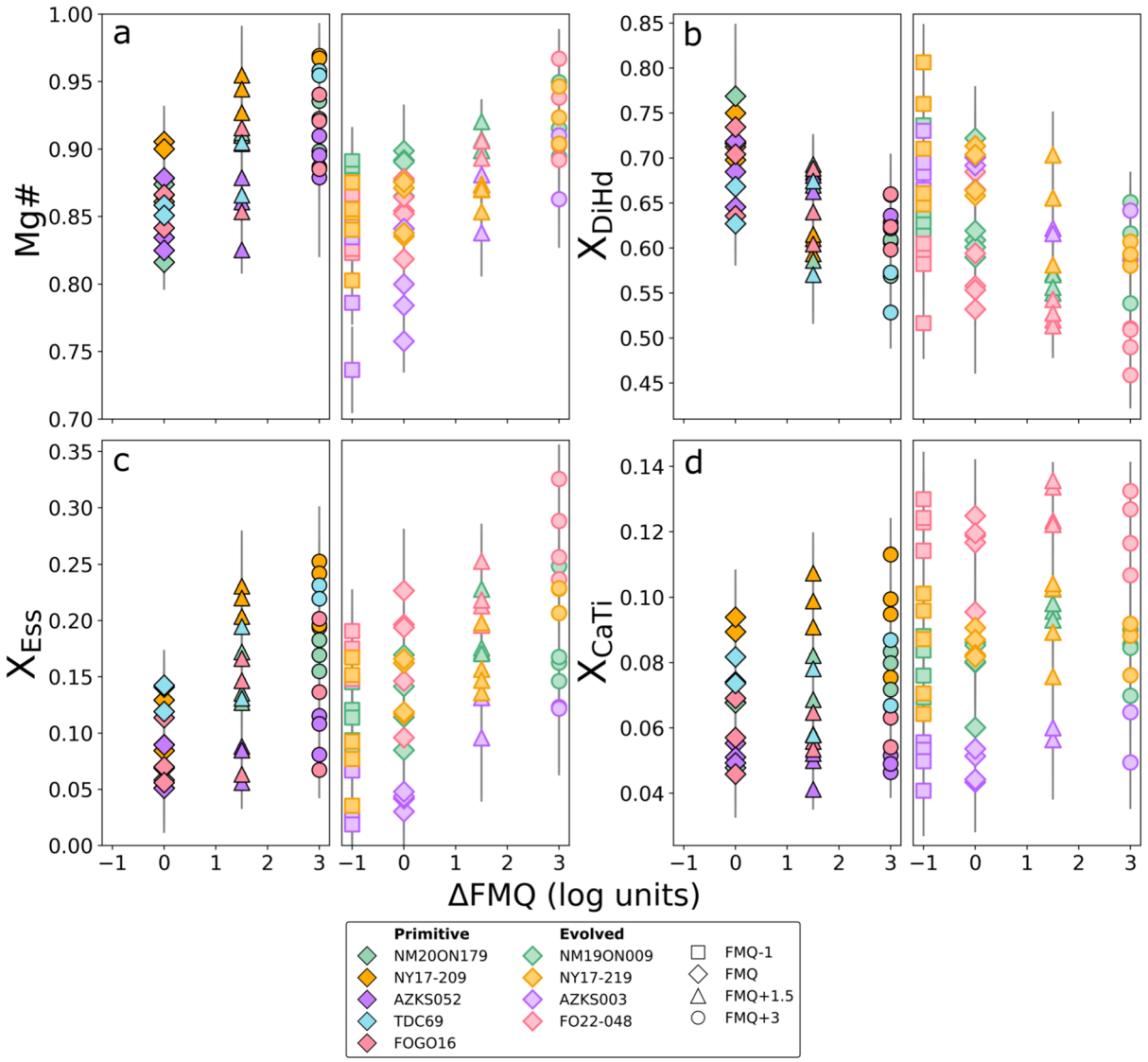

Fig. 8 Clinopyroxene components as a function of fO_2 calculated using the method of Neave et al. (2024a). **a** Mg#, where Mg# = 100 Mg/(Mg + Fe^{2+}); **b** diopside and hedenbergite, DiHd, Ca(Mg, Fe^{2+})Si_2O_6); **c** esseneite, Ess, $CaFe^{3+}AlSiO_6$; and **d** titanian calcium-Tschermak's components CaTi ($CaTiAl_2O_6$). Spread observed at each fO_2 condition for a given starting composition reflects the effect of temperature

at FMQ + 3 where no experiments were conducted close to the liquidus, there is an initial crystallisation interval in which SiO_2 contents remain stable or increase only minimally. In the primitive experiments, we begin to see the effect of prevailing redox conditions on SiO_2 at ~1140 °C, coinciding with the onset of clinopyroxene crystallisation. At FMQ, where little spinel crystallises, we observe SiO_2 depletion of up to 1.8 wt% over a temperature interval of 32 °C (Fig. S7, Supplementary Material 2). In sample NM20ON009 however, a SiO_2 enrichment of 1.1 wt% is observed. At FMQ + 1.5, all samples excluding AZKS052 show SiO_2 enrichment (Fig. S8, Supplementary Material 2), which is most extreme under the most oxidising conditions as melt fractions dwindle and the proportion of spinel increases significantly. Silica enrichment ranges between 4.8 wt% (AZKS048) and 8.0 wt% (NM20ON179) over starting composition values for primitive compositions at FMQ + 3. In the evolved experiments, liquids are progressively enriched in SiO_2 in all samples and at all fO_2 conditions. enrichment is enhanced most under oxidising conditions, after clinopyroxene crystallisation, though experiments at FMQ + 3 were not continued to low temperature to enable direct comparisons.

Both FeO and TiO_2 show similar trends at FMQ; they are progressively concentrated in primitive melts, with the effect particularly evident for TiO_2. At FMQ + 1.5, extensive spinel crystallisation leads to falling FeO (Fig. 10f), up to 2.4 wt% over a temperature interval of 21 °C, and the plateau

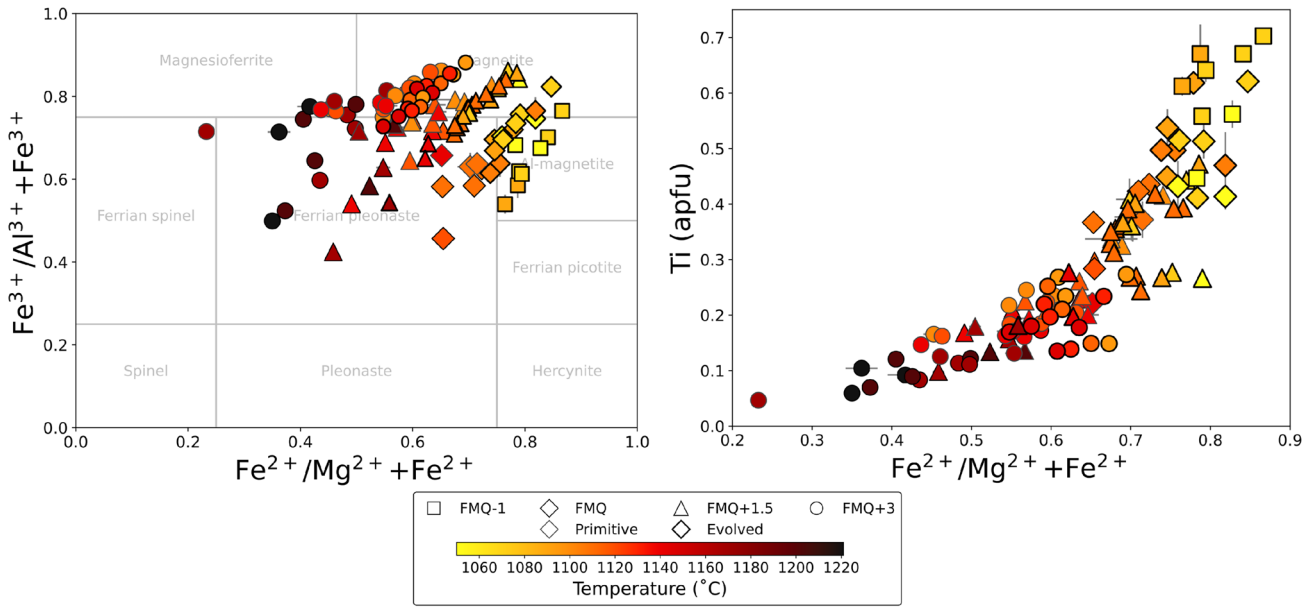

Fig. 9 Experimental spinels s.l. from both primitive and evolved experiments. **a** Binary classification diagram of Gargiulo et al. (2013) showing Fe^{2+}# vs Fe^{3+}#, and **b** binary diagram of Ti (apfu) vs Fe^{2+}#

or fall of TiO_2 in all samples excluding AZKS052. Under the most oxidising conditions, TiO_2 and FeO fall for most primitive samples. Sample AZKS052 however, saturates pseudobrookite, which strongly controls melt TiO_2 content. In this sample TiO_2 rises, reaching 4.1 wt% before pseudobrookite begins to crystallise, at which point it declines. Evolved compositions at FMQ-1 show initial increase in FeO (Fig. 10b) followed by a subsequent decrease at the onset of spinel crystallisation. This trend is replicated for TiO_2 which reaches up to 3.9 wt%, in samples AZKS003, NM19ON009 and FO22-048, all of which have ilmenite in their low temperature assemblages. In NY17-219 however, TiO_2 falls at a continuous and steady rate. As fO_2 increases, earlier spinel crystallisation in higher proportions leads to a continuously decreasing trend for both FeO and TiO_2 contents in all evolved samples, with no initial period of increasing concentrations.

Alumina displays contrasting trends that depend predominantly on starting composition and, in particular, on the alkali content. For highly alkaline compositions, we observe a steady, continuous rise in Al_2O_3 concentrations. In these compositions, plagioclase is typically absent, or only formed in minimal amounts compared to the proportion of Al-free phases. In less alkaline samples such as AZKS052 and AZKS003 however, where plagioclase is more abundant, we see Al_2O_3 increase to the point of plagioclase saturation, typically around 1140 °C, before its concentration then declines. In sample FOGO16, we see a blend of both trends, with conditions at FMQ producing the same trend as for samples AZKS052 and AZKS003, while at FMQ+1.5 Al_2O_3 concentrations plateau after plagioclase saturation, and at FMQ+3 they continue to increase. This reflects the increase in the proportion of clinopyroxene, spinel (s.l.) and Fe-Ti oxides relative to plagioclase as fO_2 increases.

Discussion

Effect of bulk composition on phase equilibria

Liquid line of descent and degree of silica-saturation

The compositions we investigated differ significantly in their degree of silica-saturation. In order to discuss the effect of silica-saturation on phase equilibria, CIPW normative components were calculated using the pyrolite python package developed by Williams et al. (2020). Melt $Fe^{3+}/\Sigma Fe$ ratios were determined using the algorithm of Kress and Carmichael (1991) by considering the nominal experimental fO_2. CIPW norm components were then used to calculate the feldspathoid silica-saturation index (FSSI) of Frost and Frost (2008), where FSSI = normative Qz − [Lc + 2(Ne + Kp)]/100. Figure 12 shows the variation of FSSI with temperature. Most starting compositions are nepheline normative, with the exception of AZKS052 and AZKS003, which are both hypersthene normative (FSSI = 0). We find that the slope of liquid lines of descent (LLDs) in Na_2O+K_2O vs SiO_2 space is in part controlled by the FSSI of the starting composition (Fig. 11a, c). The most undersaturated compositions tend to have steeper LLDs, becoming enriched in alkalis through significant crystallisation of phases that concentrate alkalis in the melt such

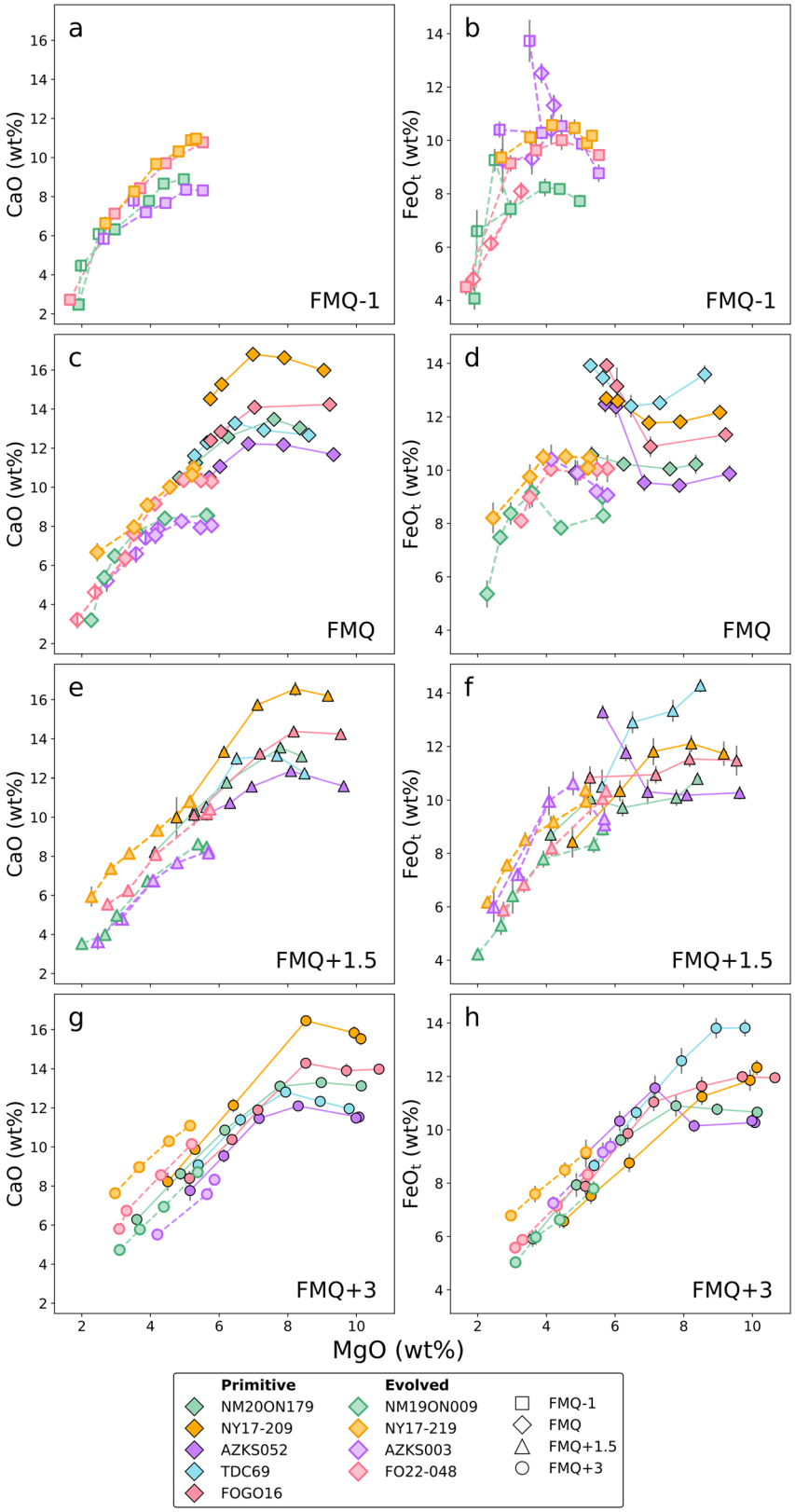

Fig. 10 Melt oxide concentrations (normalised to 100 wt%) of CaO and FeO_{tot} as a function of MgO content, for experiments using primitive (symbols with black outlines) and evolved starting compositions (symbols with coloured outlines). Half-filled symbols joined with dashed lines reflect experimental charges with bimodal glass compositions, where silica-rich components are filled on the left side of the symbol, and silica-poor components are filled on the right

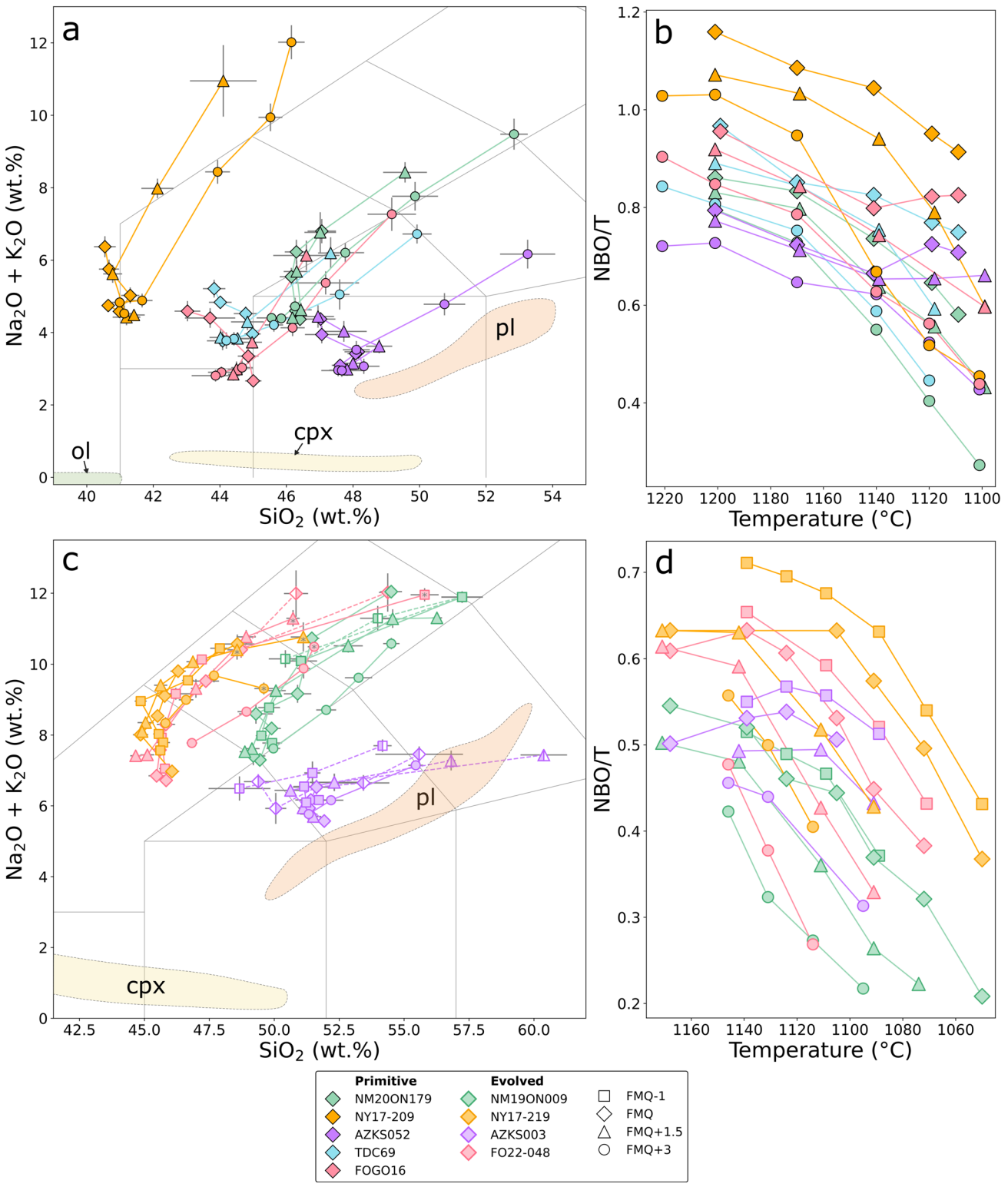

Fig. 11 Total alkalis (Na_2O+K_2O wt%) versus SiO_2 (wt%) plots and NBO/T (see discussion below for calculation method) versus temperature plots for **a**, **b** experiments using primitive compositions, **c**, **d** experiments using evolved compositions. Half-filled symbols joined with dashed lines seen in **c** reflect experimental charges with bimodal glass compositions, where silica-rich components are filled on the left side of the symbol, and silica-poor components are filled on the right. Bimodal glass compositions were excluded from **b** and **d**. Asterisks on certain evolved experiments in **c** denote those where analytical difficulties (e.g. small melt pools) meant that alkali-migration was unavoidable, and values are lower than expected. Shaded regions in **a** and **c** reflect the compositional range of olivine, clinopyroxene and plagioclase in our experiments

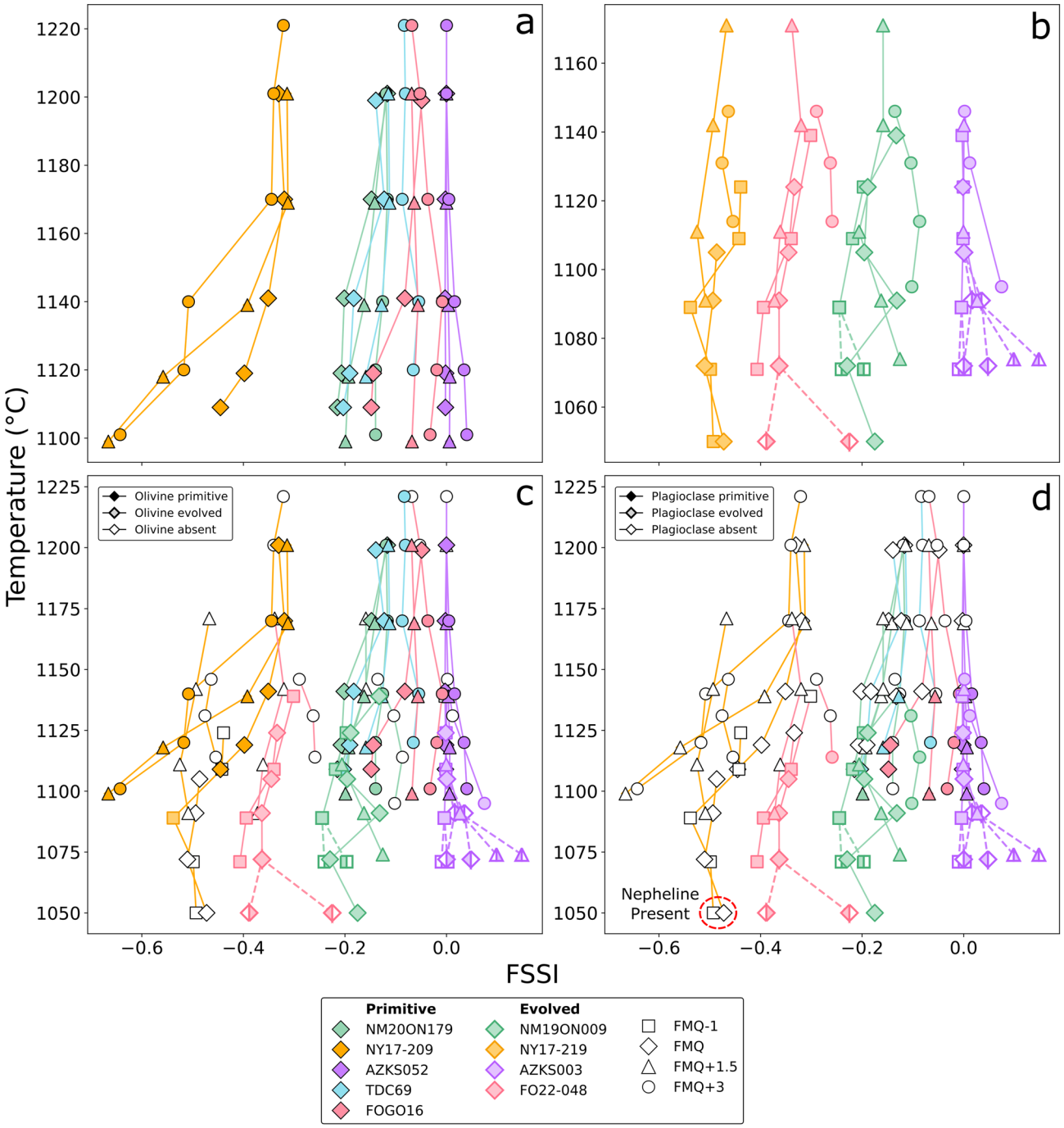

Fig. 12 Melt feldspathoid silica saturation index (FSSI) vs. temperature, where FSSI = normative Qz − [Lc + 2(Ne + Kp)]/100. **a** Experiments using primitive compositions; **b** experiments using evolved compositions; **c** experiments using primitive and evolved compositions, coloured symbols indicate presence of olivine; **d** experiments using primitive and evolved compositions, coloured symbols indicate presence of plagioclase. Circled experiments produce nepheline at 1050 °C. The mean error in calculated FSSI is 0.02, which is about the size of the symbols shown

as clinopyroxene. Silica-saturated compositions (AZKS052 and AZKS003) meanwhile, tend to crystallise higher proportions of phases such as plagioclase, in which alkalis are more compatible, and hence display much shallower trends, dominated by silica-enrichment.

Melt fractions at any given temperature are linked to the composition of the starting material. In the evolved compositions there is a trend for increasingly silica-undersaturated (i.e. low FSSI) melts, and NY17-219 in particular, to have high melt fractions. Salazar-Naranjo and Vlach (2023) also

found higher melt fractions in experiments using a basanite starting composition compared with a tephrite. A contributing factor to high melt fraction in our experiments comes from the inability of these highly-undersaturated compositions to crystallise significant quantities of plagioclase, while experimental temperatures are still too high to produce silica-undersaturated phases such as nepheline. Nepheline is only observed ~60–90 °C below the saturation temperature of plagioclase in evolved compositions.

Relationships between composition and resulting melt fraction are less clear for primitive compositions than for evolved compositions. At high temperatures, all samples have similar melt fractions, with the exception of the high-FeO (14.2 wt%) and high-MgO (1185 wt%) sample TDC69, which saturates both in olivine and spinel at higher temperatures than the other primitive compositions and at temperatures beyond the range explored in this work. After clinopyroxene saturation, melt fraction largely depends on prevailing fO_2 conditions and not as much on the experimental bulk composition.

Assessing the influence of the experimental starting composition on the degree of melt evolution across the investigated temperature range is challenging due to the multidimensional nature of the 10-component compositions. Instead, to simplify our analysis, we use the parameter NBO/T, which describes the degree of melt polymerisation (Mysen 1983) and may be used as a proxy for melt differentiation (Fig. 11b, d). NBO/T is calculated from the ratio of non-bridging oxygens to tetrahedral cations, with lower NBO/T values indicating more polymerised, differentiated melts. In calculating NBO/T, Fe^{3+} is often assumed to be a network-former alongside Si^{4+}, Al^{3+}, Ti^{4+} and P^{5+}. However, in reality it may also act as a network-modifier, depending on its coordination in the melt (Mysen 2021; Le Losq and Sossi 2023). Here we assume that all Fe^{3+} cations are network-formers. At high temperatures, silica-undersaturated compositions tend to be the least polymerised, due to lower melt SiO_2 contents, and higher proportions of alkalis and CaO, which act as network-disruptors or -modifiers (Mysen 1983, 2021; Borisov et al. 2017). Combined with their higher melt fraction, this implies that in general, very silica-undersaturated compositions can produce large volumes of relatively low-viscosity melts at a given temperature (Salazar-Naranjo and Vlach 2023), in which crystal-melt segregation may be easier, when compared with less undersaturated compositions.

The primitive group of starting compositions tend to have higher NBO/T values than their evolved counterparts, due to their lower proportion of tetrahedral cations and, with a few exceptions, NBO/T falls with temperature. Sample NY17-209, the most undersaturated primitive sample, experiences the greatest increase in polymerisation with falling temperature (Fig. 11b). As the only primitive sample not to saturate plagioclase, Al_2O_3 contents rise dramatically from 11.5 wt% in the starting material, to 18.0 wt% at 1101 °C and FMQ+3, while CaO plummets from 14.0 wt% to 8.2 wt% due to the abundant clinopyroxene crystallisation. This leads NBO/T to fall from 1.03 to 0.45 at FMQ+3. In comparison, AZKS052 shows low initial NBO/T (0.73–0.79), which falls until plagioclase saturation at ~1140 °C, at which point NBO/T either increases slightly (FMQ) or plateaus (FMQ+1.5) at around ~0.66. Only under the most oxidising conditions does this silica-saturated sample become increasingly polymerised under falling temperatures, when the increase in spinel crystallisation leads to the concentration of SiO_2 in the melt.

Evolved compositions show similar trends to the primitive compositions, with only silica saturated sample AZKS003 showing an initial increase of NBO/T at FMQ-1 and FMQ, due to early plagioclase crystallisation, which depletes the melt in the network-forming SiO_2 and Al_2O_3 (Fig. 11d). The crystallisation of plagioclase exerts a strong effect on the evolution of melt polymerization. While NM19ON009 has a lower FSSI than AZKS003, and both have similar assemblages, the proportion of plagioclase is up to 3.3 times higher in AZKS003 than NM19ON009. This results in NM19ON009, despite its much higher melt fraction at a given temperature, having a much lower NBO/T than AZKS003, whose polymerization only increases significantly at FMQ+3.

Effect of bulk composition on olivine stability

The presence of olivine depends predominantly on melt MgO and CaO contents. In the primitive experiments, as previously stated, TDC69 saturates olivine much earlier than the other samples, and in significantly higher proportions than any other sample, primitive or evolved. This is the effect of this sample's high MgO (11.8 wt.%) content, which promotes high olivine liquidus temperatures (Roeder and Emslie 1970; Sugawara 2000).

In the evolved experiments, olivine stability also depends strongly on composition, with the size of the olivine stability field inversely correlated with silica undersaturation (Fig. 12c). As silica-undersaturation increases, olivine becomes unstable under more oxidising conditions, and is absent from all experiments bar one at FMQ-1 in NY17-219, the most silica-undersaturated. Olivine stability also correlates inversely with the CaO content of the starting composition. The stability field of clinopyroxene widens while olivine is removed from the liquidus at high fO_2 conditions in our high CaO samples, an observation similarly reported by Conte et al. (2009) in their CaO doped experiments. Furthermore, the addition of P_2O_5 is suggested to

destabilise olivine at reducing conditions (Toplis et al. 1994) and FOGO16 and NY17-209, which have the highest P_2O_5 contents, tend to crystallise the lowest proportions of olivine.

Effect of bulk composition on clinopyroxene stability

Clinopyroxene saturation temperatures in the primitive experiments are typically ~20 °C higher than those in the evolved experiments. We attribute this to higher melt MgO and CaO contents in the former, which are correlated with clinopyroxene saturation temperatures (Chen and Zhang 2009; Conte et al. 2009; Romano et al. 2020).

The melt composition is also correlated with the phase proportions of clinopyroxene, with higher crystal fractions correlated with higher melt Mg#. For a given melt fraction, the crystal fraction of clinopyroxene increases with decreasing FSSI, such that the most undersaturated samples (NY17-209 and NY17-219 for experiments on primitive and evolved compositions respectively) have a mineral assemblage dominated by clinopyroxene. This effect is likely related to the high CaO contents of these compositions, where clinopyroxene crystallisation is promoted at the expense of phases such as olivine (Conte et al. 2009).

Effect of bulk composition on plagioclase stability

The timing of plagioclase saturation is tied to silica-saturation (Fig. 12d), with the most undersaturated compositions from the primitive and evolved series producing plagioclase at the lowest temperatures of their group, in lower proportions, or not at all (NY17-209, NY17-219). The suppression of plagioclase in the most SiO_2-undersaturated experiments is a consequence, primarily, of the low effective silica activity in these melts. This is captured by the simple equilibrium $NaAlSiO_4 + 2SiO_2 = NaAlSi_3O_8$, which demonstrates the higher silica requirement to form albite. As effective $aSiO_2$ decreases, the melt increasingly favours feldspathoid components relative to feldspar. This first order silica activity effect is reinforced by bulk composition controls: the most undersaturated compositions are often Ca-rich and become clinopyroxene dominated, which acts as a major sink for Ca (and some Al), reducing the stability of the anorthite component of plagioclase and contributing to its suppression in these compositions.

Strong correlations are observed between melt SiO_2, Ca# (Ca# = molar Ca/(Ca + Na)) and plagioclase An#, with low silica, high Ca# melts, such as those in the primitive series, producing more anorthitic plagioclase than those in more evolved melts (Panjasawatwong et al. 1995; Namur et al. 2012; Neave and Namur 2022).

The effect of fO_2 on phase equilibria

Effect on melt evolution

A wide range of residual glass compositions can be produced through equilibrium crystallisation by varying temperature and fO_2. The degree of silica-saturation depends strongly on redox conditions (Fig. 12), with both primitive and evolved melts evolving towards silica-enrichment at FMQ + 3. At FMQ, primitive compositions FOGO16, TDC69 and NM20ON179 produce increasingly silica-undersaturated liquids with falling temperature, evolving towards lower FSSI values. A similar result was observed by Salazar-Naranjo and Vlach (2023), who performed comparable experiments on a basanite and tephrite at 1 atm. In our evolved compositions, however, there is no clear distinction in terms of silica-saturation trends between experiments between FMQ-1 and FMQ + 1.5. Only at FMQ + 3 do we see a distinct evolutionary trend towards higher FSSI values.

The most silica-undersaturated primitive starting composition, NY17-209, is an outlier, with increasing fO_2 promoting silica-depletion, rather than enrichment. From the major element data (Figs. S7–S9, Supplementary Material 2), we see a rapid increase in alkali contents with decreasing temperatures at the highest fO_2 conditions in this composition. The crystal assemblage of NY17-209 is dominated by clinopyroxene (crystal fractions up to 51.9 wt%, the highest of any sample), concentrating alkalis in the melt while depleting it in silica. High melt $Fe^{3+}/\Sigma Fe$ (see below) limits the crystallisation of olivine, which would otherwise enrich the melt in silica, along with the crystallisation of spinel, and the melt evolves towards lower FSSI.

In addition to compositional controls, melt fraction also depends strongly on prevailing fO_2. Specifically, melt fraction falls with increasing fO_2, thus producing more evolved residual melts at any given temperature. These melts subsequently have the lowest NBO/T, due to their enrichment in tetrahedral cations. Plotting melt evolution on the TAS diagram (Fig. 11a) reveals distinct LLDs for each fO_2 condition for primitive starting compositions, where silica enrichment increasingly dominates over alkalis as fO_2 increases. The origin of the divergence in LLDs is clearer in Fig. 12. At high temperatures, FSSI values are similar at all fO_2 conditions. FSSI values only begin to deviate significantly at ~1140 °C, which coincides with the onset of clinopyroxene crystallisation. Depleting melt silica contents and enriching alkali contents produces more silica-undersaturated melts at FMQ. At higher fO_2, the onset of clinopyroxene crystallisation is associated with an increase of spinel crystal fraction, as clinopyroxene concentrates FeO_{tot} and TiO_2 in the melt. The incompatibility of both alkalis and silica in spinel leads

to the production melts with high alkali contents but also, critically, high silica contents, with higher FSSI values.

Experiments on evolved compositions meanwhile do not show distinct LLDs for each fO_2 condition. Much like the trends observed in FSSI, we observe similar LLDs on the TAS-diagram (Fig. 11c) at FMQ-1 to FMQ+1.5. Unlike clinopyroxene in primitive experiments, evolved clinopyroxenes do not act to deplete melt silica, and typically contain FeO_{tot} at concentrations comparable to the starting materials. This means that they do not enrich the melt in FeO_{tot} to the same extent as clinopyroxenes in experiments on primitive compositions. Crystal fractions of spinel are therefore similar at conditions lower than FMQ+3 and we observe similar LLDs on the TAS-diagram. It is only the significant increase in spinel crystal fraction that occurs at FMQ+3 that promotes higher FSSI values and produces distinct LLDs that are silica-enriched relative to those at lower fO_2 (Fig. 10b).

The abundance of Fe^{3+} (Fig. S10, Supplementary Material 2) in the melt also depends on the degree of silica-undersaturation. As FSSI decreases, the $Fe^{3+}/\Sigma Fe$ ratio increases, with the effect being strongest at the highest fO_2. This results from the addition of Na_2O, found in the highest concentrations in the most undersaturated compositions, and lower melt silica content, both of which increase equilibrium $Fe^{3+}/\Sigma Fe$ (Thy and Lofgren 1994; Borisov et al. 2013, 2017). This in turn influences the crystallising assemblage, most significantly for Fe-bearing phases. The stability field of olivine, whose crystallisation increases melt silica and alkalis, shrinks with increasing melt $Fe^{3+}/\Sigma Fe$ due to its dependence on the activity of Fe^{2+} in the melt, crystallising in smaller fractions as conditions become more oxidising. We also observe that ilmenite is replaced by pseudobrookite as melts become more oxidising due to its Fe^{3+}-rich composition (Mullen and McCallum 2013).

The crystal fraction of clinopyroxene in experiments performed on primitive compositions increases significantly with fO_2, while fractions are less variable in their evolved counterparts. Unlike the low-pressure clinopyroxenes of Salazar-Naranjo and Vlach (2023), clinopyroxenes produced in our experiments on primitive compositions have higher silica contents than the starting material at all fO_2 conditions, most significantly at lower fO_2. At FMQ, where the crystal fraction of spinel is low, the onset of clinopyroxene crystallisation depletes melt silica contents, an effect enhanced by silica-rich plagioclase in some samples. This is still the case at FMQ+1.5 for composition AZKS052, whose mineral assemblage is dominated by plagioclase, with little spinel. Evolved compositions produce clinopyroxenes with silica contents comparable to or slightly lower than their respective starting materials. Increased clinopyroxene crystallisation at higher fO_2 for primitive and evolved compositions alike, predominantly acts to concentrate alkalis in the melt, while depleting melt CaO.

It is well recorded that redox conditions strongly control the saturation of spinel (s.l.) and Fe-Ti oxides (e.g. Toplis and Carroll 1995; Zhang et al. 2023). Higher liquidus temperatures, and enhanced spinel crystallisation, induces silica- and alkali-enrichment in the melt during crystallisation under oxidising conditions, while depleting it in FeO_{tot}. In experiments using primitive starting compositions, the crystal fraction of spinel is widely variable. At FMQ crystal fractions are less than 1.2%, while at FMQ+3 they reach up to 11.5%, and this variability is predominantly responsible for the variable LLDs we observe. Comparatively, in experiments using evolved starting compositions, the spread in spinel fractions is much lower, and crystal fractions only increase significantly at FMQ+3. This difference is in part due to the lower availability of Fe in evolved compositions, which have lower bulk FeO_{tot}, alongside higher P_2O_5 contents.

Our results demonstrate the highly diverse range of liquid lines of descent that can be produced through variations in fO_2 and bulk composition alone. Despite this, we were unable to produce any of our natural, evolved starting compositions, through crystallisation of a primitive one, indicating other factors such as pressure and crustal assimilation may play an important role.

Olivine-melt Fe–Mg exchange coefficients

Beyond controlling the evolution of the liquid itself, fO_2 strongly influences apparent Fe–Mg exchange equilibria between minerals and melts. For ferromagnesian minerals, this is mainly a reflection of the melt $Fe^{3+}/\Sigma Fe$ (Kress and Carmichael 1991; Borisov et al. 2018) ratio, as well as the amount of Fe^{3+} incorporated into the mineral structure (e.g. Neave et al. 2024a, b).

Our experiments also cover a large range of fO_2 conditions when compared with natural variability (Fig. 1), and a wide range of melt composition. We can therefore independently investigate the role of both of these parameters in controlling mineral-melt Fe–Mg equilibria.

Figure S11 (Supplementary Material 2) clearly demonstrates the strong dependency of olivine-melt Fe–Mg exchange coefficients on both the melt $Fe^{3+}/\Sigma Fe$ ratio (Fig. S11a) and the melt composition, decreasing with increasing silica undersaturation (Fig. S11b) (Mysen 2006; Borisov and McCammon 2010; Putirka 2016; Borisov et al. 2017; Saper et al. 2022). These observations are related to the effect of melt $Fe^{3+}/\sum Fe$ on melt structure (Mysen 2006) and the activity of components such as FeO in the melt, which is known to increase with alkali content (O'Neill 2021; Saper et al. 2022). After calculating melt $Fe^{3+}/\Sigma Fe$ using

the algorithm of Kress and Carmichael (1991), we obtain $K_{D_{Fe^{2+}-Mg}}^{Ol-Melt}$ values ranging between 0.20–0.35 for primitive experiments and 0.27–0.34 for evolved experiments. These values exclude those experiments with bimodal melt compositions, or those where alkali loss occurred due to analytical difficulties (i.e. reduced beam size during measurement). We also examined partition coefficients $D_{Mg}^{Ol-melt}$ (primitive compositions 4.83–13.34; evolved compositions 7.49–16.19) and $D_{Fe^{2+}}^{Ol-melt}$ (primitive compositions 1.29–3.43; evolved compositions 2.20–5.43) which show a non-linear correlation with NBO/T (Fig. S12).

Accurate equilibrium K_D values are critical for many petrological calculations, including the assessment of equilibrium in both natural and experimental samples, fractionation modelling, and correcting for post entrapment crystallisation in olivine-hosted melt inclusions. Several models exist for estimating of equilibrium K_D values, including those of Toplis (2005), Putirka (2016) and Blundy et al. (2020), which are calibrated on a wide range of compositions. The models of Toplis (2005) and Putirka (2016) parameterise $K_{D_{Fe^{2+}-Mg}}^{Ol-Melt}$, while that of Blundy et al. (2020) parameterizes $K_{D_{Fe^{T}-Mg}}^{Ol-Melt}$, with the two related by the expression $K_{D_{Fe^{T}-Mg}}^{Ol-Melt} = K_{D_{Fe^{2+}-Mg}}^{Ol-Melt} \times (1 - \frac{Fe^{3+}}{\Sigma Fe})$. Here we apply these three models to our experiments (n = 100) and low-pressure experimental data on alkali systems from the literature (n = 139), in order to assess their use specifically on alkaline compositions. This combined dataset of our experiments and those from the literature spans a temperature range of 1049–1330 °C, fO_2 conditions from FMQ-1 to FMQ + 3, melt SiO_2 from 38.3–60.1 wt% and total alkali content from 2.4–14.2 wt%.

The Toplis (2005) model (Fig. 13a), which places particular emphasis on the role of alkalis, has an $R^2 = 0.37$ and average absolute deviation (a.a.d) of 0.024 when applied to our data, and typically overestimates experimentally derived values. Blundy et al. (2020) suggest that part of the compositional dependence described by Toplis (2005), may stem from shortcomings in the algorithm used to calculate $Fe^{3+}/\Sigma Fe$ in capturing the parameters compositional dependence. These authors instead calibrate a model based on a dataset of 52 experiments where $Fe^{3+}/\Sigma Fe$ has been measured in the glass, which they assess using a literature compilation in which $Fe^{3+}/\Sigma Fe$ is calculated using the model of Borisov et al. (2018). When applied to our data, we obtain a poor fit, with $R^2 = 0.03$ and a.a.d. = 0.035. The authors note that the calibration is best suited for compositions with $Na_2O + K_2O < 8$ wt%, and R^2 and a.a.d. improve to 0.42 and 0.026 respectively when the model is applied to compositions that fulfil this constraint. The Borisov et al. (2018) model for calculating melt $Fe^{3+}/\Sigma Fe$ typically returns lower values than the models of Kress and Carmichael (1991), Putirka (2016) and Sun and Yao (2024) (Fig. S1, Supplementary Material 2) for our experiments, and is likely one source of the overestimation of $K_{D_{Fe^{T}-Mg}}^{Ol-Melt}$ seen in Fig. 13c. The effect of model choice on melt $Fe^{3+}/\Sigma Fe$ is discussed further in Supplementary Material 2, where we compare the median estimates for $K_{D_{Fe^{2+}-Mg}}^{Ol-Melt}$ using each of these four models for calculating melt $Fe^{3+}/\Sigma Fe$, and observe increased variability between estimates as fO_2 increases.

Equation 8c of Putirka (2016), was fitted to describe the data of Gee and Sack (1988), where melts are highly silica-undersaturated. It is therefore not surprising that this model has the best fit for our data out of models currently available in the literature, with $R^2 = 0.60$ and a.d.d. = 0.019. All three models discussed here are reliant on the experiments of Sack et al. (1987) and Gee and Sack (1988), performed at FMQ, to calibrate models for use on silica-undersaturated alkaline compositions. Our suite of experiments therefore provide an opportunity to calibrate a new model for the estimation of K_D in alkaline compositions, across a range of fO_2 conditions.

In order to build our own parametrisation, we randomly split the combined dataset of our experiments and those from the literature into training (n = 167) and test (n = 72) datasets, and compared multiple least squares regression models for both $K_{D_{Fe^{T}-Mg}}^{Ol-Melt}$ and $K_{D_{Fe^{2+}-Mg}}^{Ol-Melt}$, with different combinations of variables. Following the approach of Putirka et al. (2003), we first checked for variable t-ratios > 5, and selected models with the highest F-ratios, to avoid overfitting our data. We then further tested to see if our variables were truly independent using the variance inflation factor (VIF), where values above 10 are indicative of multicollinearity (i.e. variables are correlated with each other). We then applied these models to the test dataset to assess model reliability, and calculate R^2 and a.a.d. values.

We initially developed a model based on the observed relationship between silica-undersaturation (Fig. S11b, Supplementary Material 2) and $K_{D_{Fe^{2+}-Mg}}^{Ol-Melt}$. However, using FSSI as a parameter obscures relationships between melt composition and K_D. In light of this, we explored simpler parameterisations using melt composition directly. We found we could produce a similar fit to our initial model using compositional parameters X_{SiO_2} and $(X_{Na_2O} + X_{K_2O})/X_{SiO_2}$ in place of FSSI:

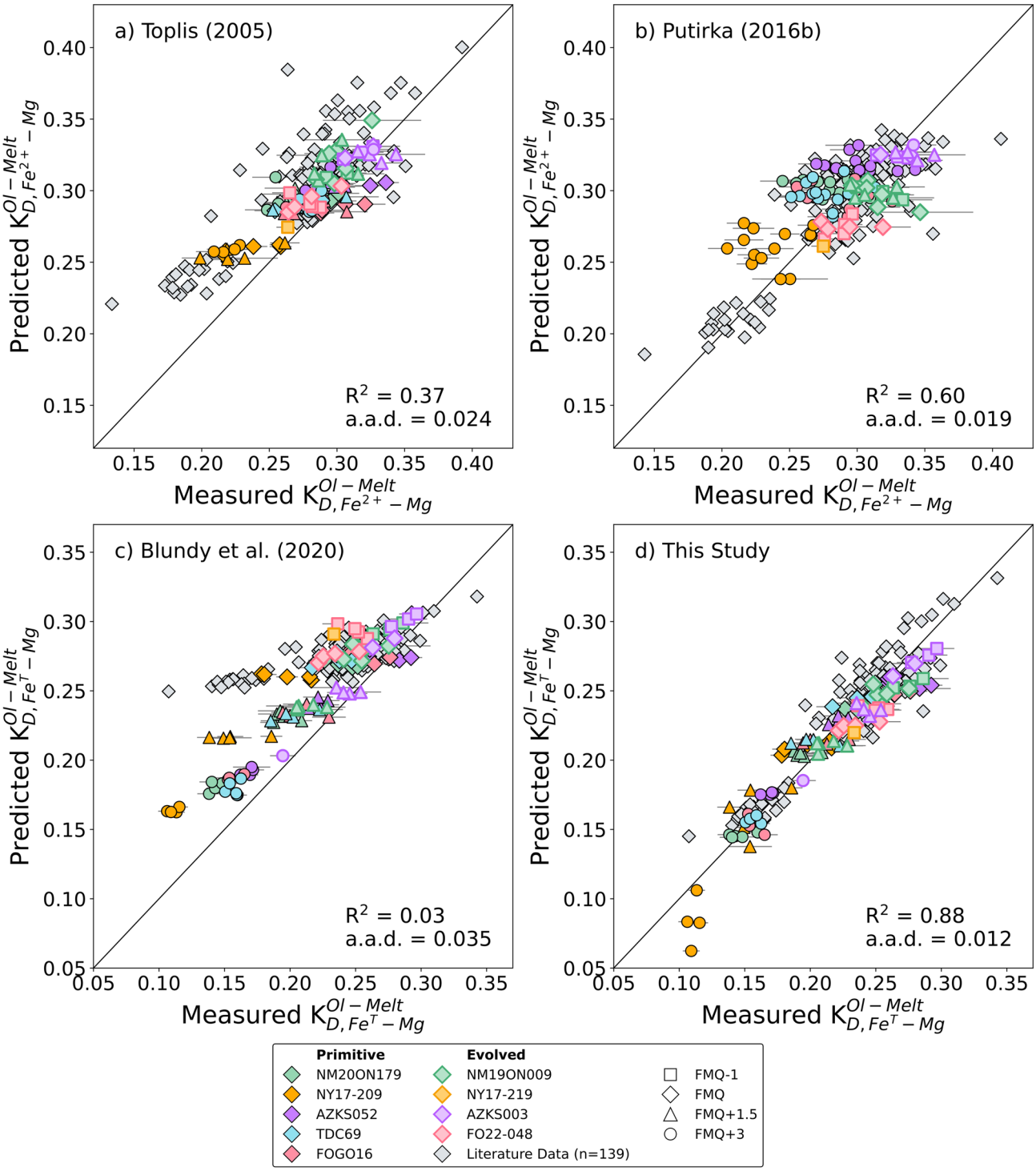

Fig. 13 Predicted vs measured $K_{D_{Fe-Mg}}^{Ol-Melt}$ values using **a** Toplis (2005), **b** Equation 8d, Putirka (2016), **c** Blundy et al. (2020), **d** Eq. 2 for our experiments on primitive (n = 67) and evolved (n = 33) compositions, and those from the literature (n = 139, from: Mahood and Baker 1986; Sack et al. 1987; Gee and Sack 1988; Kennedy et al. 1990; Thy 1991; Gerke et al. 2005). $Fe^{3+}/\Sigma Fe$ were calculated using **a** Kilinc et al. (1983) plus a term for P_2O_5 taken from Toplis et al. (1994), **b** Equation 6b, Putirka (2016), **c** Borisov et al. (2018), **d** Kress and Carmichael (1991)

$$K_{D_{Fe^{2+}-Mg}}^{Ol-Melt} = 0.338\,(\pm0.034) + 0.355\,(\pm0.41)\,[X_{SiO_2}] - 0.538\,(\pm0.031)\left[\frac{X_{Na_2O}+X_{K_2O}}{X_{SiO_2}}\right] - 0.216\,(\pm0.023)\,[X_{Fo}] \quad (1)$$

where X_i is the mole fraction of i in the melt and X_{Fo} is molar MgO/(MgO+FeO) of olivine. When applied to our test dataset we obtain $R^2=0.77$ and a.a.d.=0.014, and $R^2=0.78$ and a.a.d.=0.015 when applied to the dataset as a whole (Fig. S13).

We then tested a similar model in which $K_{D_{Fe^{T}-Mg}}^{Ol-Melt}$ is parameterised instead,, enabling comparison with the model of Blundy et al. (2020). The final regression was:

$$K_{D_{Fe^{T}-Mg}}^{Ol-Melt} = 0.442\,(\pm0.029) + 0.287\,(\pm0.035)\,[X_{SiO_2}] - 0.442\,(\pm0.027)\left[\frac{X_{Na_2O}+X_{K_2O}}{X_{SiO_2}}\right] - 0.168\,(\pm0.022)\,[X_{Fo}] - 0.138(\pm0.008)\frac{1}{(1-\left[\frac{Fe^{3+}}{\Sigma Fe}\right])} \quad (2)$$

where$Fe^{3+}/\Sigma Fe$ was calculated using the equation of Kress and Carmichael (1991). We obtain $R^2=0.89$ and a.a.d.=0.011 when applied to our test dataset, and $R^2=0.88$ and a.a.d.=0.012 when applied to the dataset as a whole (Fig. 12d). The higher R^2 values obtained compared with Eq. 1 are the result of making the dependence of K_D on $Fe^{3+}/\sum Fe$ explicit.

These models provide a significant improvement over currently available models for estimating equilibrium $K_{D_{Fe^{2+}-Mg}}^{Ol-Melt}$ and $K_{D_{Fe^{T}-Mg}}^{Ol-Melt}$ in alkaline magmas at low pressure. We do not evaluate their performance at high pressure, though the effect of pressure is estimated to be small (Toplis 2005; Blundy et al. 2020; Saper et al. 2022). We therefore suggest our new equations may still provide useful initial estimates of K_D for alkaline magmas at crustal pressures.

Clinopyroxene-melt Fe–Mg exchange coefficients

Unlike olivine, a lack of prior experimental work has meant the parameters governing clinopyroxene-melt Fe–Mg exchange equilibria, are less clear, particularly in alkaline systems (Neave et al. 2024a, b). Clinopyroxene-melt K_D values in our experiments are highly variable, and depend on both composition (Fig. 14a, c) and redox conditions (Fig. 14b). The effect of sector zoning further obscures these relationships, due to the preferential incorporation of MgO in hourglass sectors, and FeO in prism sectors in our experiments, and hence higher K_D values are recorded by prism sectors than hourglass sectors. Where possible we measured a balanced selection of each type of sector, though our experimental clinopyroxenes were generally small, and measurements were often mixed.

$K_{D_{Fe^{2+}-Mg}}^{Cpx-Melt}$ values observed in our experiments vary between 0.07–0.30, where clinopyroxene Fe^{3+} is estimated using the method of Droop (1987), as recommended by Neave et al. (2024a, b). Individual compositions define more limited ranges in $K_{D_{Fe^{2+}-Mg}}^{Cpx-Melt}$, with the lowest values belonging to the most silica-undersaturated compositions. These values are much lower than the mean of 0.245±0.008 proposed by Salazar-Naranjo and Vlach (2023), which we attribute to the limited range of starting compositions explored. Our values are similar however to those reported by Molendijk et al. (2023) (0.04–0.34), whose experiments were performed on similar, highly-undersaturated compositions and under similar conditions.

When calculated as $K_{D_{Fe^{T}-Mg}}^{Cpx-Melt}$, we obtain average values of 0.27±0.06 at FMQ-1 and FMQ, falling in the suggested range of Putirka (2008). At FMQ+1.5, average $K_{D_{Fe^{T}-Mg}}^{Cpx-Melt}$ is 0.36±0.10, and 0.46±0.14 at FMQ+3. Salazar-Naranjo and Vlach (2023) propose an average of 0.37±0.03 for experiments at FMQ>1, which is in agreement with our results at FMQ+1.5. Our standard deviations are much higher however, due to the wider range of compositions considered.

Several authors have previously calibrated models for the prediction of $K_{D_{Fe^{T}-Mg}}^{Cpx-Melt}$ (e.g. Putirka 2008; Bédard 2010), with the assumption that all Fe is present as Fe^{2+}. Such models do not reflect the ability of clinopyroxene to incorporate both Fe^{2+} and Fe^{3+} in its crystal structure, nor the high melt $Fe^{3+}/\Sigma Fe$ that is observed in alkaline magmas, and hence produce poor results when applied to these systems.

While our experiments were not designed to evaluate iron speciation in clinopyroxene, and are limited by mixed measurements of different sectors, we were able to use our data to build a simple linear regression model for the estimation of $K_{D_{Fe^{T}-Mg}}^{Cpx-Melt}$ that incorporates the effect of melt $Fe^{3+}/\Sigma Fe$, using a similar approach to that used for olivine above. We calibrated the model on individual clinopyroxene measurements from our experiments, which cover the range: T=1050–1170 °C; fO_2=FMQ-1 − FMQ+3; Mg#=0.54–0.85. We split out measurements into training (n=806) and testing (n=346) datasets, and then further tested on the mean values from each experiment (n=63). The final regression was:

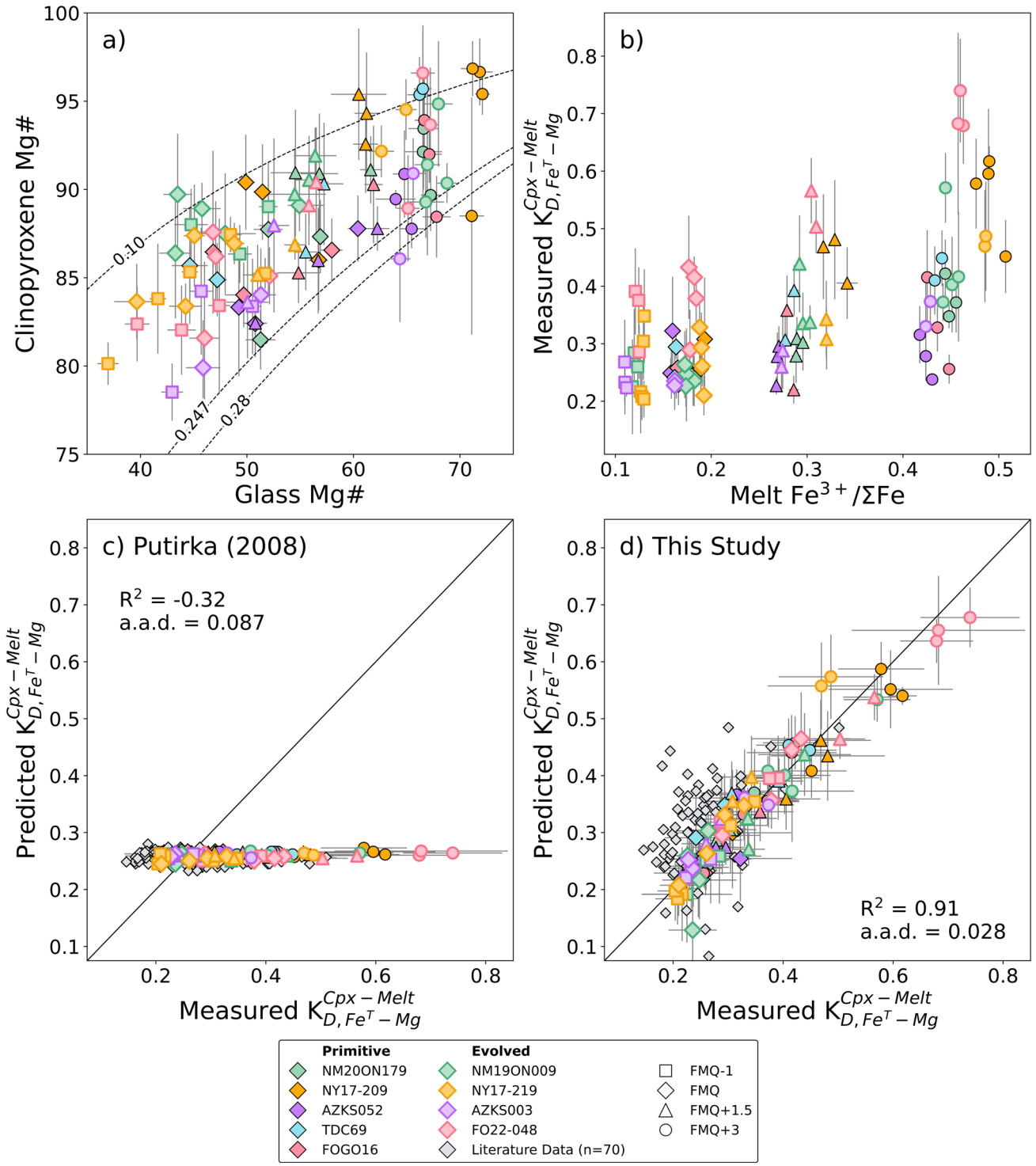

Fig. 14 **a** Rhodes diagram for experimental clinopyroxenes. Dashed lines indicate different values of $K_{D_{Fe^{2+}-Mg}}^{Cpx-Melt}$. Clinopyroxene Mg# is calculated using Fe^{2+} values obtained via the method of Droop (1987), while glass Mg# is calculated using Fe^{2+} contents obtained using the algorithm of Kress and Carmichael (1991) and the experimental fO_2, **b** $K_{D_{Fe^T-Mg}}^{Cpx-Melt}$ versus calculated melt $Fe^{3+}/\Sigma Fe$, **c** predicted vs measured $K_{D_{Fe^{2+}-Mg}}^{Cpx-Melt}$ using Eq. 35 of Putirka (2008), **d** predicted vs measured $K_{D_{Fe^T-Mg}}^{Cpx-Melt}$ values using Eq. 2 for our experiments on primitive (n=42) and evolved (n=57) compositions, where points reflect the average $K_{D_{Fe^T-Mg}}^{Cpx-Melt}$ and error bars are 1σ. Literature clinopyroxenes (n=70, from: Mahood and Baker 1986; Sack et al. 1987; Gee and Sack 1988; Kennedy et al. 1990; Thy 1991; Gerke et al. 2005; Molendijk et al. 2023; Salazar-Naranjo and Vlach 2023) are also shown for comparison, but not used to evaluate model performance due to less precise analytical methods

$$K_{D_{Fe^T-Mg}}^{Cpx-Melt} = -1.00\,(\pm 0.064) + 2.129\,(\pm 0.063)\left[\frac{T\ (^\circ C)}{1000}\right] - 1.675\,(\pm 0.021)\,[Mg\#] + 0.144(\pm 0.006)\frac{1}{(1-\left[\frac{Fe^{3+}}{\Sigma Fe}\right])} \quad (3)$$

where T is the temperature in degrees Celsius, Mg# is molar MgO/(MgO+FeO_{tot}) of clinopyroxene and melt $Fe^{3+}/\Sigma Fe$ was calculated using the equation of Kress and Carmichael (1991). When applied to our test dataset we obtain $R^2=0.89$ and a.a.d.=0.030 and $R^2=0.92$ and a.a.d.=0.028 when applied to the dataset as a whole. When compared with Eq. 35 of Putirka (2008), which results in $R^2=-0.32$ (i.e. the model performs worse than using the mean as the predicted value) and a.d.d.=0.087 when applied to our mean clinopyroxene measurements, the fit of Eq. 3 is substantially better, with $R^2=0.91$ and a.d.d.=0.028 (Fig. 14d). We further apply Eq. 3 to clinopyroxene-melt pairs from the literature (n=70) (Fig. 14d), however we do not evaluate the performance of our model on this data due to less precise analytical methods (i.e. lower beam current, short counting times) and few analyses per experiment.

Equation 3 provides an improved estimate of $K_{D_{Fe^T-Mg}}^{Cpx-Melt}$ in alkaline magmas, by accounting for the effects of melt $Fe^{3+}/\Sigma Fe$, however further work is still needed. Experiments targeted at understanding both Fe^{2+} and Fe^{3+} partitioning between clinopyroxene and melt, and the effects of disequilibrium crystallisation will enable us to more accurately predict $K_{D_{Fe^{2+}-Mg}}^{Cpx-Melt}$, and unlock the potential for clinopyroxene as a recorder of magmatic redox conditions.

Conclusions

This experimental study explored the influence of bulk composition and fO_2 on phase equilibria and liquid lines of descent in alkali basalts. Experiments were performed at 1 atm on nine natural starting compositions, in the temperature range 1220–1050 °C, and at fO_2 conditions from FMQ-1 to FMQ+3.

We find that fO_2 is the dominant control over phase stability and melt evolution. The influence of fO_2 on the Fe^{3+}/Fe_{tot} ratio of the melt, controls the composition and stability of Fe-bearing phases, whose crystallisation determines the subsequent evolutionary trajectory of the melt. Specifically, at lower fO_2, melt evolution is predominantly controlled by the crystallisation of phases such as clinopyroxene, which is close in silica content to the melt, but contains fewer alkalis, driving the melt towards alkali enrichment. At high fO_2 increased crystallisation of clinopyroxene and the destabilisation of olivine are observed, however the critical factor is the promotion of early spinel (s.l.) crystallisation. With increasing fO_2, evolutionary trajectories become comparatively enriched in silica, with respect to alkalis, producing less silica-undersaturated melts.

Bulk composition plays a secondary role, modulating the extent to which fO_2 conditions control melt evolution. The liquid lines of descent of primitive melts, which contain greater concentrations of redox sensitive elements such as Fe in the bulk composition, are more easily influenced by changes in fO_2, with distinct evolutionary paths observed at each fO_2 condition investigated. Comparatively, evolved compositions show similar LLDs at low to moderately oxidising conditions, and only the most oxidising promote silica enrichment. With increasing silica-undersaturation, the slope of LLDs in Na_2O+K_2O vs SiO_2 space also becomes steeper, towards more alkali enriched compositions. Melt fraction at a given temperature increases, NBO/T decreases, and mineral assemblages become dominated by clinopyroxene, while plagioclase is absent. Olivine stability is decreased in evolved melts compared to primitive, as well as at higher fO_2.

Mineral-melt exchange coefficients ($K_{D_{Fe^{2+}-Mg}}^{Mineral-Melt}$) are also compositionally dependent, on both the mineral and the melt. In both olivine and clinopyroxene, K_D is correlated with silica-saturation; $K_{D_{Fe^{2+}-Mg}}^{Mineral-Melt}$ values decrease as melts become more silica-undersaturated, the effect particularly strong in olivine. Based on this observation, we propose new equations for the estimation of equilibrium olivine $K_{D_{Fe^{2+}-Mg}}^{Ol-Melt}$ and $K_{D_{Fe^T-Mg}}^{Ol-Melt}$ in alkaline compositions, which use melt SiO_2, Na_2O and K_2O contents, and olivine forsterite content, in addition to melt $Fe^{3+}/\Sigma Fe$ in the latter. These models ($K_{D_{Fe^{2+}-Mg}}^{Ol-Melt}$: $R^2=0.78$ and a.a.d.=0.015; $K_{D_{Fe^T-Mg}}^{Ol-Melt}$: $R^2=0.90$ and a.a.d.=0.011), represent a significant improvement over existing models for these compositions. We additionally present a simple model for the estimation of $K_{D_{Fe^T-Mg}}^{Cpx-Melt}$ in alkaline systems that incorporates the effect of melt $Fe^{3+}/\Sigma Fe$, as well as temperature and clinopyroxene Mg#, recovering $R^2=0.92$ and a.a.d.=0.029. These new models are applicable for a wide range of temperatures, fO_2 conditions and compositions, enabling more accurate assessment of mineral-melt equilibrium in alkaline systems.

Finally, this new suite of experiments on alkali basalts may prove useful in calibrating new empirical and thermodynamic models, and thermodynamic datasets for alkaline systems. These are vital for understanding natural volcanic

systems, and further refinement is needed to address their current weaknesses.

Supplementary Information The online version contains supplementary material available at https://doi.org/10.1007/s00410-026-02309-w.

Acknowledgements We thank Y. Zhang for assistance with microprobe analyses. SYMT was supported by a KU Leuven C1 (C14/20/062) grant. ON acknowledges support from Fonds Wetenschappelijk Onderzoek through an Odysseus grant. DAN acknowledges support from National Environmental Research Council (NE/T011106/1). BC is a Senior Research Associate of the Belgian Fund for Scientific Research-FNRS. We thank Etienne Médard and Manuel Pimenta Silva, and handling editor Othmar Müntener for their constructive reviews which significantly improved the quality of this manuscript.

Author contributions SYMT—project design, data acquisition, writing; ON—project design, acquisition of funding, supervision, writing; DAN—writing; BC—writing; JB – data acquisition, SK—editing.

Data availability EPMA data is available in the Supplementary Materials.

Declarations

Conflict of interest The authors declare no competing interests.

References

Andersen DJ, Lindsley DH, Davidson PM (1993) QUILF: A Pascal program to assess equilibria among Fe-Mg-Mn-Ti oxides, pyroxenes, olivine, and quartz. Comput Geosci 19:1333–1350

Anderson AT (1968) The oxygen fugacity of alkaline basalt and related magmas, Tristan da Cunha. Am J Sci 266:704–727

Batanova VG, Thompson JM, Danyushevsky LV et al (2019) New olivine reference material for in situ microanalysis. Geostand Geoanal Res 43:453–473. https://doi.org/10.1111/ggr.12266

Beard CD, Goodenough KM, Borst AM et al (2023) Alkaline-silicate REE-HFSE systems. Econ Geol 118:177–208. https://doi.org/10.5382/econgeo.4956

Bédard JH (2010) Parameterization of the Fe = Mg exchange coefficient (Kd) between clinopyroxene and silicate melts. Chem Geol 274:169–176. https://doi.org/10.1016/j.chemgeo.2010.04.003

Berndt J, Koepke J, Holtz F (2005) An experimental investigation of the influence of water and oxygen fugacity on differentiation of MORB at 200 MPa. J Petrol 46:135–167. https://doi.org/10.1093/petrology/egh066

Blundy J, Melekhova E, Ziberna L et al (2020) Effect of redox on Fe–Mg–Mn exchange between olivine and melt and an oxybarometer for basalts. Contrib Mineral Petrol 175:103. https://doi.org/10.1007/s00410-020-01736-7

Borisov A, McCammon C (2010) The effect of silica on ferric/ferrous ratio in silicate melts: an experimental study using Mössbauer spectroscopy. Am Mineral 95:545–555. https://doi.org/10.2138/am.2010.3217

Borisov A, Behrens H, Holtz F (2013) The effect of titanium and phosphorus on ferric/ferrous ratio in silicate melts: an experimental study. Contrib Mineral Petrol 166:1577–1591. https://doi.org/10.1007/s00410-013-0943-9

Borisov A, Behrens H, Holtz F (2017) Effects of strong network modifiers on Fe^{3+}/Fe^{2+} in silicate melts: an experimental study. Contrib Mineral Petrol 172:34. https://doi.org/10.1007/s00410-017-1337-1

Borisov A, Behrens H, Holtz F (2018) Ferric/ferrous ratio in silicate melts: a new model for 1 atm data with special emphasis on the effects of melt composition. Contrib Mineral Petrol 173:98. https://doi.org/10.1007/s00410-018-1524-8

Bosi F, Biagioni C, Pasero M (2019) Nomenclature and classification of the spinel supergroup. Eur J Mineral 31:183–192. https://doi.org/10.1127/ejm/2019/0031-2788

Brounce M, Stolper E, Eiler J (2017) Redox variations in Mauna Kea lavas, the oxygen fugacity of the Hawaiian plume, and the role of volcanic gases in Earth's oxygenation. Proc Natl Acad Sci USA 114:8997–9002. https://doi.org/10.1073/pnas.1619527114

Charlier B, Grove TL (2012) Experiments on liquid immiscibility along tholeiitic liquid lines of descent. Contrib Mineral Petrol 164:27–44. https://doi.org/10.1007/s00410-012-0723-y

Charlier B, Namur O, Grove TL (2013) Compositional and kinetic controls on liquid immiscibility in ferrobasalt–rhyolite volcanic and plutonic series. Geochim Cosmochim Acta 113:79–93. https://doi.org/10.1016/j.gca.2013.03.017

Chase MW Jr, Davies CA, Downey JR Jr et al (1985) JANAF thermochemical tables. J Phys Chem Ref Data 14(Suppl 1):535

Chen Y, Zhang Y (2009) Clinopyroxene dissolution in basaltic melt. Geochim Cosmochim Acta 73:5730–5747. https://doi.org/10.1016/j.gca.2009.06.016

Connors L, Wallace PJ, Sims KWW et al (2025) Magma sources, crustal storage depths, and degassing of alkalic, CO_2-rich magmas at Nyiragongo and Nyamulagira Volcanoes, Democratic Republic of the Congo. Earth Planet Sci Lett 665:119477. https://doi.org/10.1016/j.epsl.2025.119477

Conte AM, Dolfi D, Gaeta M et al (2009) Experimental constraints on evolution of leucite-basanite magma at 1 and 10−4 GPa: implications for parental compositions of Roman high-potassium magmas. Eur J Mineral 21:763–782. https://doi.org/10.1127/0935-1221/2009/0021-1934

Cottrell E, Kelley KA (2011) The oxidation state of Fe in MORB glasses and the oxygen fugacity of the upper mantle. Earth Planet Sci Lett 305:270–282. https://doi.org/10.1016/j.epsl.2011.03.014

Cottrell E, Birner SK, Brounce M et al (2021) Oxygen fugacity across tectonic settings. In: Magma redox geochemistry. American Geophysical Union (AGU), pp 33–61 https://doi.org/10.1002/9781119473206.ch3

DeVitre CL, Gazel E, Ramalho RS et al (2023) Oceanic intraplate explosive eruptions fed directly from the mantle. Proc Natl Acad Sci USA 120:e2302093120. https://doi.org/10.1073/pnas.2302093120

Droop GTR (1987) A general equation for estimating Fe^{3+} concentrations in ferromagnesian silicates and oxides from microprobe analyses, using stoichiometric criteria. Mineral Mag 51:431–435. https://doi.org/10.1180/minmag.1987.051.361.10

Duke J (1971) The effect of variation of oxygen fugacity on the crystallization of an alkali basalt from the Azores. McGill University , Montreal

Erdmann M, Koepke J (2016) Experimental temperature cycling as a powerful tool to enlarge melt pools and crystals at magma storage conditions. American Mineralogist 101:960–969. https://doi.org/10.2138/am-2016-5398

Feig ST, Koepke J, Snow JE (2010) Effect of oxygen fugacity and water on phase equilibria of a hydrous tholeiitic basalt. Contrib Mineral Petrol 160:551–568. https://doi.org/10.1007/s00410-010-0493-3

Frost BR (1991) Introduction to oxygen fugacity and its petrologic importance. In: Lindsley DH (ed) Oxide minerals: petrologic and magnetic significance. De Gruyter, Berlin, pp 1–10

Frost BR, Frost CD (2008) A geochemical classification for feldspathic igneous rocks. J Petrol 49:1955–1969. https://doi.org/10.1093/petrology/egn054

Gargiulo MF, Bjerg EA, Mogessie A (2013) Spinel group minerals in metamorphosed ultramafic rocks from Río de Las Tunas belt, Central Andes, Argentina. Geol Acta 11:133–148

Gee LL, Sack RO (1988) Experimental petrology of melilite nephelinites. J Petrol 29:1233–1255. https://doi.org/10.1093/petrology/29.6.1233

Gerke TL, Kilinc AI, Sack RO (2005) Ti-content of high-Ca pyroxenes as a petrogenetic indicator: an experimental study of mafic alkaline rocks from the Mt. Erebus volcanic region, Antarctica. Contrib Mineral Petrol 148:735–745. https://doi.org/10.1007/s00410-004-0636-5

Ghiorso MS, Sack RO (1995) Chemical mass transfer in magmatic processes IV. A revised and internally consistent thermodynamic model for the interpolation and extrapolation of liquid-solid equilibria in magmatic systems at elevated temperatures and pressures. Contrib Mineral Petrol 119:197–212. https://doi.org/10.1007/BF00307281

Goodenough KM, Schilling J, Jonsson E et al (2016) Europe's rare earth element resource potential: an overview of REE metallogenetic provinces and their geodynamic setting. Ore Geol Rev 72:838–856. https://doi.org/10.1016/j.oregeorev.2015.09.019

Hamada M, Fujii T (2007) H_2O-rich island arc low-K tholeiite magma inferred from Ca-rich plagioclase-melt inclusion equilibria. Geochem J 41:437–461. https://doi.org/10.2343/geochemj.41.437

Hamilton DL, Burnham CW, Osborn EF (1964) The solubility of water and effects of oxygen fugacity and water content on crystallization in mafic magmas. J Petrol. https://doi.org/10.1093/petrology/5.1.21

Head E, Lanzirotti A, Newville M, Sutton S (2018) Vanadium, sulfur, and iron valences in melt inclusions as a window into magmatic processes: a case study at Nyamuragira Volcano, Africa. Geochim Cosmochim Acta 226:149–173. https://doi.org/10.1016/j.gca.2018.01.033

Hildner E, Klügel A, Hansteen TH (2012) Barometry of lavas from the 1951 eruption of Fogo, Cape Verde Islands: implications for historic and prehistoric magma plumbing systems. J Volcanol Geotherm Res 217–218:73–90. https://doi.org/10.1016/j.jvolgeores.2011.12.014

Hill R, Roeder P (1974) The crystallization of spinel from basaltic liquid as a function of oxygen fugacity. J Geol 82:709–729. https://doi.org/10.1086/628026

Honma U (2012) Hydrous and anhydrous melting experiments of an alkali basalt and a transitional tholeiite from the Oginosen Volcano, Southwest Japan: the possible influence of melt depolymerization on Ca-Na partitioning between plagioclase and the melt. J Mineral Petrol Sci 107:8–32. https://doi.org/10.2465/jmps.091126

Honour VC, Holness MB, Partridge JL, Charlier B (2019) Microstructural evolution of silicate immiscible liquids in ferrobasalts. Contrib Mineral Petrol 174:77. https://doi.org/10.1007/s00410-019-1610-6

Jarosewich E, Nelen JA, Norberg JA (1980) Reference samples for electron microprobe analysis*. Geostand Newsl. https://doi.org/10.1111/j.1751-908X.1980.tb00273.x

Jeffery AJ, Gertisser R (2018) Peralkaline felsic magmatism of the Atlantic Islands. Front Earth Sci 6:145. https://doi.org/10.3389/feart.2018.00145

Kamate Kaleghetso E, Namur O, Smets B et al (2025) Magmatic differentiation and plumbing system beneath Nyamulagira Volcano (Virunga Volcanic Province, East African Rift). J Volcanol Geotherm Res 458:108264. https://doi.org/10.1016/j.jvolgeores.2024.108264

Kennedy AK, Grove TL, Johnson RW (1990) Experimental and major element constraints on the evolution of lavas from Lihir Island, Papua New Guinea. Contrib Mineral Petrol 104:722–734. https://doi.org/10.1007/BF01167289

Kilinc A, Carmichael ISE, Rivers ML, Sack RO (1983) The ferric-ferrous ratio of natural silicate liquids equilibrated in air. Contr Mineral and Petrol 83:136–140. https://doi.org/10.1007/BF00373086

Klügel A, Day S, Schmid M, Faria B (2020) Magma plumbing during the 2014–2015 eruption of Fogo (Cape Verde Islands). Front Earth Sci 8:157. https://doi.org/10.3389/feart.2020.00157

Kouchi A, Sugawara Y, Kashima K, Sunagawa I (1983) Laboratory growth of sector zoned clinopyroxenes in the system $CaMgSi_2O_6$-$CaTiAl_2O_6$. Contrib Mineral Petrol 83:177–184. https://doi.org/10.1007/BF00373091

Kress VC, Carmichael ISE (1991) The compressibility of silicate liquids containing Fe_2O_3 and the effect of composition, temperature, oxygen fugacity and pressure on their redox states. Mineral and Petrol 108:82–92. https://doi.org/10.1007/BF00307328

Le Bas MJ, Le Maitre RW, Streckeisen A et al (1986) A chemical classification of volcanic rocks based on the total alkali-silica diagram. J Petrol 27:745–750. https://doi.org/10.1093/petrology/27.3.745

Le Losq C, Sossi PA (2023) Atomic structure and physical properties of peridotite glasses at 1 bar. Front Earth Sci. https://doi.org/10.3389/feart.2023.1040750

Le Roex AP, Cliff RA, Adair BJI (1990) Tristan da Cunha, South Atlantic: geochemistry and petrogenesis of a basanite-phonolite lava series. J Petrol 31:779–812. https://doi.org/10.1093/petrology/31.4.779

Longhi J (1990) Silicate liquid immiscibility in isothermal crystallization experiments. In: Lunar and planetary science conference, 20th, pp 13–24

MacDonald A, Ubide T, Mollo S et al (2023) The influence of undercooling and sector zoning on clinopyroxene–melt equilibrium and thermobarometry. J Petrol 64:egad074. https://doi.org/10.1093/petrology/egad074

Mahood GA, Baker DR (1986) Experimental constraints on depths of fractionation of mildly alkalic basalts and associated felsic rocks: Pantelleria, Strait of Sicily. Contrib Mineral Petrol 93:251–264. https://doi.org/10.1007/BF00371327

Markl G, Marks MAW, Frost BR (2010) On the controls of oxygen fugacity in the generation and crystallization of peralkaline melts. J Petrol 51:1831–1847. https://doi.org/10.1093/petrology/egq040

Marxer F, Ulmer P (2019) Crystallisation and zircon saturation of calc-alkaline tonalite from the Adamello Batholith at upper crustal conditions: an experimental study. Contrib Mineral Petrol 174:84. https://doi.org/10.1007/s00410-019-1619-x

Marxer F, Ulmer P, Müntener O (2022) Polybaric fractional crystallisation of arc magmas: an experimental study simulating transcrustal magmatic systems. Contrib Mineral Petrol 177:3. https://doi.org/10.1007/s00410-021-01856-8

Masotta M, Pontesilli A, Mollo S et al (2020) The role of undercooling during clinopyroxene growth in trachybasaltic magmas: insights on magma decompression and cooling at Mt. Etna volcano. Geochim Cosmochim Acta 268:258–276. https://doi.org/10.1016/j.gca.2019.10.009

Mata J, Martins S, Mattielli N et al (2017) The 2014–15 eruption and the short-term geochemical evolution of the Fogo volcano (Cape Verde): evidence for small-scale mantle heterogeneity. Lithos 288–289:91–107. https://doi.org/10.1016/j.lithos.2017.07.001

Molendijk SM, Namur O, Mason PRD et al (2023) Trace element partitioning in silica-undersaturated alkaline magmatic systems. Geochim Cosmochim Acta 346:29–53. https://doi.org/10.1016/j.gca.2023.01.025

Molendijk SM, Namur O, Kamate Kaleghetso E et al (2024) Plumbing system architecture and differentiation processes of the Nyiragongo Volcano, DR Congo. J Petrol 65:egad088. https://doi.org/10.1093/petrology/egad088

Mollo S, Putirka K, Iezzi G et al (2011) Plagioclase–melt (dis)equilibrium due to cooling dynamics: implications for thermometry, barometry and hygrometry. Lithos 125:221–235. https://doi.org/10.1016/j.lithos.2011.02.008

Mollo S, Putirka K, Misiti V et al (2013) A new test for equilibrium based on clinopyroxene–melt pairs: clues on the solidification temperatures of Etnean alkaline melts at post-eruptive conditions. Chem Geol 352:92–100. https://doi.org/10.1016/j.chemgeo.2013.05.026

Moretti R, Neuville DR (2021) Redox equilibria. In: Magma redox geochemistry. American Geophysical Union (AGU), pp 1–17 https://doi.org/10.1002/9781119473206.ch1

Morimoto N (1988) Nomenclature of pyroxenes. Mineral Petrol 39:55–76. https://doi.org/10.1007/BF01226262

Moussallam Y, Longpré M-A, McCammon C et al (2019) Mantle plumes are oxidised. Earth Planet Sci Lett 527:115798. https://doi.org/10.1016/j.epsl.2019.115798

Mullen EK, McCallum IS (2013) Coexisting pseudobrookite, ilmenite, and titanomagnetite in hornblende andesite of the Coleman Pinnacle flow, Mount Baker, Washington: evidence for a highly oxidized arc magma. Am Mineral 98:417–425. https://doi.org/10.2138/am.2013.4185

Müntener O, Kelemen PB, Grove TL (2001) The role of H_2O during crystallization of primitive arc magmas under uppermost mantle conditions and genesis of igneous pyroxenites: an experimental study. Contrib Mineral Petrol 141:643–658. https://doi.org/10.1007/s004100100266

Mysen BO (1983) The structure of silicate melts. Annu Rev Earth Planet Sci 11:75. https://doi.org/10.1146/annurev.ea.11.050183.000451

Mysen BO (2006) Redox equilibria of iron and silicate melt structure: implications for olivine/melt element partitioning. Geochim Cosmochim Acta 70:3121–3138. https://doi.org/10.1016/j.gca.2006.03.014

Mysen B (2021) Structure of chemically complex silicate systems. In: Encyclopedia of glass science, technology, history, and culture. Wiley, pp 197–206 https://doi.org/10.1002/9781118801017.ch2.6

Namur O, Charlier B, Toplis MJ, Vander Auwera J (2012) Prediction of plagioclase-melt equilibria in anhydrous silicate melts at 1-atm. Contrib Mineral Petrol 163:133–150. https://doi.org/10.1007/s00410-011-0662-z

Neave DA, Namur O (2022) Plagioclase archives of depleted melts in the oceanic crust. Geology 50:848–852. https://doi.org/10.1130/G49840.1

Neave DA, Bali E, Guðfinnsson GH et al (2019) Clinopyroxene–liquid equilibria and geothermobarometry in natural and experimental tholeiites: the 2014–2015 Holuhraun Eruption, Iceland. J Petrol 60:1653–1680. https://doi.org/10.1093/petrology/egz042

Neave DA, Stewart AG, Hartley ME, McCammon C (2024a) Re-evaluating stoichiometric estimates of iron valence in magmatic clinopyroxene crystals. Contrib Mineral Petrol 179:5. https://doi.org/10.1007/s00410-023-02080-2

Neave DA, Stewart AG, Hartley ME, Namur O (2024b) Iron valence systematics in clinopyroxene crystals from ocean island basalts. Contrib Mineral Petrol 179:67. https://doi.org/10.1007/s00410-024-02144-x

Nekvasil H, Dondolini A, Horn J et al (2004) The origin and evolution of silica-saturated alkalic suites: an experimental study. J Petrology 45:693–721. https://doi.org/10.1093/petrology/egg103

Nicklas RW, Hahn RKM, Willhite LN et al (2022) Oxidized mantle sources of HIMU- and EM-type ocean island basalts. Chem Geol 602:120901. https://doi.org/10.1016/j.chemgeo.2022.120901

O'Neill HSC (1987) Quartz-fayalite-iron and quartz-fayalite-magnetite equilibria and the free energy of formation of fayalite (Fe_2SiO_4) and magnetite (Fe_3O_4). Am Mineral 72:67–75

O'Neill HSC (2021) The thermodynamic controls on sulfide saturation in silicate melts with application to ocean floor basalts. In: Magma redox geochemistry. American Geophysical Union (AGU), pp 177–213 https://doi.org/10.1002/9781119473206.ch10

Osborn EF (1959) Role of oxygen pressure in the crystallization and differentiation of basaltic magma. Am J Sci 257:609–647

Panjasawatwong Y, Danyushevsky LV, Crawford AJ, Harris KL (1995) An experimental study of the effects of melt composition on plagioclase-melt equilibria at 5 and 10 kbar: implications for the origin of magmatic high—an plagioclase. Contrib Mineral Petrol 118:420–432. https://doi.org/10.1007/s004100050024

Pilet S, Ulmer P, Villiger S (2010) Liquid line of descent of a basanitic liquid at 1.5 Gpa: constraints on the formation of metasomatic veins. Contrib Mineral Petrol 159:621–643. https://doi.org/10.1007/s00410-009-0445-y

Pontesilli A, Masotta M, Nazzari M et al (2019) Crystallization kinetics of clinopyroxene and titanomagnetite growing from a trachybasaltic melt: new insights from isothermal time-series experiments. Chem Geol 510:113–129. https://doi.org/10.1016/j.chemgeo.2019.02.015

Putirka K (1999) Clinopyroxene + liquid equilibria to 100 kbar and 2450 K. Contrib Mineral Petrol 135:151–163. https://doi.org/10.1007/s004100050503

Putirka KD (2008) Thermometers and barometers for volcanic systems. Rev Mineral Geochem 69:61–120. https://doi.org/10.2138/rmg.2008.69.3

Putirka K (2016) Rates and styles of planetary cooling on Earth, Moon, Mars, and Vesta, using new models for oxygen fugacity, ferric-ferrous ratios, olivine-liquid Fe-Mg exchange, and mantle potential temperature. Am Mineral 101:819–840. https://doi.org/10.2138/am-2016-5402

Putirka KD, Mikaelian H, Ryerson F, Shaw H (2003) New clinopyroxene-liquid thermobarometers for mafic, evolved, and volatile-bearing lava compositions, with applications to lavas from Tibet and the Snake River Plain, Idaho. Am Mineral 88:1542–1554. https://doi.org/10.2138/am-2003-1017

Roeder PL, Emslie RF (1970) Olivine-liquid equilibrium. Contrib Mineral Petrol 29:275–289. https://doi.org/10.1007/BF00371276

Romano P, Scaillet B, White JC et al (2020) Experimental and thermodynamic constraints on mineral equilibrium inpantelleritic magmas. Lithos 376–377:105793. https://doi.org/10.1016/j.lithos.2020.105793

Sack RO, Walker D, Carmichael ISE (1987) Experimental petrology of alkalic lavas: constraints on cotectics of multiple saturation in natural basic liquids. Contrib Mineral Petrol 96:1–23. https://doi.org/10.1007/BF00375521

Salazar-Naranjo AF, Vlach SRF (2023) New experimental constraints for the evolution and thermobarometry of alkali ultrabasic to intermediate igneous rocks. J Petrol 64:egad078. https://doi.org/10.1093/petrology/egad078

Saper LM, Baker MB, Stolper EM (2022) Fe^{2+}–Mg partitioning between olivine and liquid at low oxygen fugacity: an experimental and thermodynamic framework. Contrib Mineral Petrol 177:94. https://doi.org/10.1007/s00410-022-01955-0

Shepherd K (2024) Differentiation processes in basalts: a natural and experimental study. Dissertation, KU Leuven

Sisson TW, Grove TL (1993) Experimental investigations of the role of H_2O in calc-alkaline differentiation and subduction zone magmatism. Contrib Mineral Petrol 113:143–166. https://doi.org/10.1007/BF00283225

Snyder D, Carmichael ISE, Wiebe RA (1993) Experimental study of liquid evolution in an Fe-rich, layered mafic intrusion: constraints of Fe-Ti oxide precipitation on the T-fO_2 and T-ϱ paths of

tholeiitic magmas. Contrib Mineral Petrol 113:73–86. https://doi.org/10.1007/BF00320832

Soderman CR, Weller OM, Copley A et al (2025) Petrogenesis of cogenetic silica-undersaturated and -oversaturated rocks: quantifying the role of crustal assimilation. Earth Planet Sci Lett 667:119516. https://doi.org/10.1016/j.epsl.2025.119516

Sossi PA, Klemme S, O'Neill HStC et al (2019) Evaporation of moderately volatile elements from silicate melts: experiments and theory. Geochim Cosmochim Acta 260:204–231. https://doi.org/10.1016/j.gca.2019.06.021

Sugawara T (2000) Empirical relationships between temperature, pressure, and MgO content in olivine and pyroxene saturated liquid. J Geophys Res Solid Earth 105:8457–8472. https://doi.org/10.1029/2000JB900010

Sun C, Yao L (2024) Redox equilibria of iron in low- to high-silica melts: a simple model and its applications to C-H-O-S degassing. Earth Planet Sci Lett 638:118742. https://doi.org/10.1016/j.epsl.2024.118742

Thy P (1991) High and low pressure phase equilibria of a mildly alkalic lava from the 1965 Surtsey eruption: experimental results. Lithos 26:223–243. https://doi.org/10.1016/0024-4937(91)90030-O

Thy P, Lofgren GE (1994) Experimental constraints on the low-pressure evolution of transitional and mildly alkalic basalts: the effect of Fe-Ti oxide minerals and the origin of basaltic andesites. Contr Mineral Petrol 116:340–351. https://doi.org/10.1007/BF00306502

Toplis MJ (2005) The thermodynamics of iron and magnesium partitioning between olivine and liquid: criteria for assessing and predicting equilibrium in natural and experimental systems. Contrib Mineral Petrol 149:22–39. https://doi.org/10.1007/s00410-004-0629-4

Toplis MJ, Carroll MR (1995) An experimental study of the influence of oxygen fugacity on Fe-Ti oxide stability, phase relations, and mineral—melt equilibria in ferro-basaltic systems. J Petrol 36:1137–1170. https://doi.org/10.1093/petrology/36.5.1137

Toplis MJ, Carroll MR (1996) Differentiation of ferro-basaltic magmas under conditions open and closed to oxygen: implications for the Skaergaard Intrusion and other natural systems. J Petrol 37:837–858. https://doi.org/10.1093/petrology/37.4.837

Toplis MJ, Libourel G, Carroll MR (1994) The role of phosphorus in crystallisation processes of basalt: an experimental study. Geochim Cosmochim Acta 58:797–810. https://doi.org/10.1016/0016-7037(94)90506-1

Tormey DR, Grove TL, Bryan WB (1987) Experimental petrology of normal MORB near the Kane Fracture Zone: 22°–25° N, Mid-Atlantic Ridge. Contr Mineral and Petrol 96:121–139. https://doi.org/10.1007/BF00375227

Ubide T, Mollo S, Zhao J et al (2019) Sector-zoned clinopyroxene as a recorder of magma history, eruption triggers, and ascent rates. Geochim Cosmochim Acta 251:265–283. https://doi.org/10.1016/j.gca.2019.02.021

Ulmer P, Kaegi R, Müntener O (2018) Experimentally derived intermediate to silica-rich arc magmas by fractional and equilibrium crystallization at 1·0 GPa: an evaluation of phase relationships, compositions, liquid lines of descent and oxygen fugacity. J Petrol 59:11–58. https://doi.org/10.1093/petrology/egy017

Villiger S, Ulmer P, Müntener O (2007) Equilibrium and fractional crystallization experiments at 0·7 GPa; the effect of pressure on phase relations and liquid compositions of tholeiitic magmas. J Petrol 48:159–184. https://doi.org/10.1093/petrology/egl058

Weller OM, Holland TJB, Soderman CR et al (2024) New thermodynamic models for anhydrous alkaline-silicate magmatic systems. J Petrol 65:egae098. https://doi.org/10.1093/petrology/egae098

Willhite LN, Arevalo R Jr., Piccoli P et al (2024) Oxygen fugacity of global ocean island basalts. Geochem Geophys Geosyst 25:e2023GC011249. https://doi.org/10.1029/2023GC011249

Williams MJ, Schoneveld L, Mao Y et al (2020) Pyrolite: Python for geochemistry. J Open Source Softw 5:2314. https://doi.org/10.21105/joss.02314

Zhang Y, Namur O, Charlier B (2023) Experimental study of high-Ti and low-Ti basalts: liquid lines of descent and silicate liquid immiscibility in large igneous provinces. Contrib Mineral Petrol 178:7. https://doi.org/10.1007/s00410-022-01990-x